International Journal of Fatigue 181 (2024) 108123

Contents lists available at ScienceDirect

International Journal of Fatigue

journal homepage: www.elsevier.com/locate/ijfatigue

The influence of energy density on the low cycle fatigue behaviour of laser powder bed fused stainless steel 316L

Rory Douglas [a], William Beard [a,b], Nicholas Barnard [a], Seungjong Lee [d], Shuai Shao [c,d], Nima Shamsaei [c,d], Thomas Jones [b], Robert Lancaster [a,*]

[a] Institute of Structural Materials, Bay Campus, Swansea University, Swansea SA1 8EN, United Kingdom
[b] Rolls-Royce plc., Kings Place, 90 York Way, London N1 9FX, United Kingdom
[c] National Center for Additive Manufacturing Excellence (NCAME), Auburn University, Auburn, AL 36849, USA
[d] Department of Mechanical Engineering, Auburn University, Auburn, AL 36849, USA

ARTICLE INFO

Keywords:
Laser Powder Bed Fusion (LPBF)
Low Cycle Fatigue (LCF)
Stainless steel 316L
Energy density
Surface roughness
Build orientation

ABSTRACT

Laser powder bed fusion (LPBF) is an additive manufacturing (AM) process capable of single-step fabrication of intricate and complex structures. However, there are multiple engineering challenges associated with the introduction of AM based parts into functional industrial applications due to the lack of understanding of the role that process parameters have on the structural integrity of additively manufactured (AM) components and the subsequent effect this has on the mechanical behaviour of such materials when subjected to cyclic loading conditions. The present work will investigate the low cycle fatigue (LCF) behaviour of LPBF stainless steel 316L components manufactured with different process parameters sets and how this effects the material built in different orientations and the resulting impact this has on the material's resistance to cyclic deformation. The LCF results are supported by microstructural, fractographic and advanced surface profilometry assessments to investigate the key parameters that control the resulting fatigue performance across three different build orientations. Finally, the generated mechanical data has also been interpreted through empirical fatigue lifing models, and the various data sets have been successfully correlated to enable an estimation of longer fatigue lives.

1. Introduction

For several decades, austenitic stainless steels have been recognised for their favourable properties that make them suitable materials for multiple industrial applications [1]. In particular, stainless steel 316L (SS316L) is one of the most studied alloys from this class of materials due to the excellent mechanical properties, good machinability and excellent resistance to corrosion and oxidative processes that the alloy has to offer [2].

Historically, SS316L has been widely manufactured by conventional production techniques such as casting and forging. However using such methods can lead to strong limitations on the creation of complex geometries and the excessive cost of material removal through subsequent machining [3]. Such issues have heralded the development of additive manufacturing (AM) processes, which consist of a series of manufacturing approaches capable of net- and near-net shape production of components for industrial use. Post processing such as hot isostatic pressing (HIP) or polishing may be necessary, but overall, AM can offer a cost effective and simpler process to manufacture complex parts, whilst offering the potential of weight saving and reducing the number of process induced stress-raising features.

One of the main limitations of AM processes are related to productivity [4], since the production rates to produce a fully optimised structure are currently too low to be considered for realistic mass production. Typically, a fully-optimised process aims to produce a homogenous, high strength component with a suitable surface finish, whilst limiting the process time to save on lead time and cost. One of the obstacles to this is the sheer quantity of processing parameters that need to be balanced in the process, each impacting the properties of the final part in significant or subtle ways. These include pre-manufacture parameters such as the powder specifications, inert gas type, oxygen level,

* Corresponding author.
E-mail addresses: 862472@swansea.ac.uk (R. Douglas), william.beard@rolls-rolls.com (W. Beard), n.c.barnard@swansea.ac.uk (N. Barnard), azl0169@auburn.edu (S. Lee), sshao@auburn.edu (S. Shao), shamsaei@auburn.edu (N. Shamsaei), thomas.jones2@rolls-royce.com (T. Jones), r.j.lancaster@swansea.ac.uk (R. Lancaster).

https://doi.org/10.1016/j.ijfatigue.2023.108123
Received 9 October 2023; Received in revised form 22 December 2023; Accepted 24 December 2023
Available online 26 December 2023

Nomenclature

b	Fatigue Strength Exponent
c	Fatigue Ductility Exponent
E	Young's Modulus (GPa)
$E^{'}$	Total Volumetric Energy Density (J/mm^3)
ε_a	Strain Amplitude (mm/mm)
ε_{MAX}	Maximum Strain (mm/mm)
$\frac{\Delta\varepsilon}{2}$	Total Strain Amplitude (mm/mm)
$\frac{\Delta\varepsilon_e}{2}$	Elastic Strain Amplitude (mm/mm)
$\frac{\Delta\varepsilon_p}{2}$	Plastic Strain Amplitude (mm/mm)
$\varepsilon^{'}_f$	Fatigue Ductility Coefficient
h	Hatch Spacing/Distance (mm)
ΔJ_{eff}	Effective Elastic-Plastic Energy Release Rate (MPa-mm)
K_t	Stress Concentration Factor
n	Change in Stress State ($n = 1$ for shear and $n = 2$ for tension),
N_f	Number of Fatigue Cycles to Failure
P	Laser Power (W)
ρ_{10}	10-point Valley Radii (average radius of a micro-notch at the surface (μm))
R	Ratio of minimum to maximum strain
R_a	Average Roughness Profile (μm)
R_t	Total Height of Roughness Profile (μm)
R_p	Maximum Profile Peak Height (μm)
R_v	Maximum Depth of the Profile Below the Mean Line within the Sampling Length (μm)
R_z	The Average Values of the Heights of Five Highest-Profile Peaks and the Depths of Five Deepest Valleys Within the Sampling Length (μm)
$\Delta\sigma$	Stabilised Stress Range (MPa)
t	Layer Thickness (mm)
v	Laser Scan Speed (mm/s)

Abbreviations

0°	Horizontally Built
45°	Diagonally Built
90°	Vertically Built
AM	Additive Manufactured
EBSD	Electron Backscattered Diffraction
EDM	Electric Discharge Machining
HCF	High Cycle Fatigue
HED	High Energy Density
HIP	Hot Isostatic Pressing
IPF	Inverse Pole Figure
LPBF	Laser Powder Bed Fusion
LCF	Low Cycle Fatigue
LED	Low Energy Density
LoF	Lack of Fusion
PH	Precipitation Hardened
PSD	Powder Size Distribution
S-N	Stress/Strain Life
SEM	Scanning Electron Microscopy
SS316L	Stainless Steel 316L

and preheating temperature of the baseplate. Then, for the laser manufacturing process itself, a whole new range of parameters need to be considered, some of which include laser power, scan speed, laser spot size, laser wavelength, pulsed or constant power, layer thickness, powder distribution technique, scan route and hatch distance, all of which can be controlled [5]. Each of these parameters need careful consideration and achieving a favourable balance for manufacture requires another step in the AM process.

For laser control the significant parameters of laser power, scan speed, hatch distance and layer thickness can be combined to form a term for volumetric energy density ($E^{'}$) [6] through the relationship:

$$E^{'} = \frac{P}{v^{*}h^{*}l} \tag{1}$$

where $E^{'}$ is the total volumetric energy density (J/mm^3), P is the laser power (W), v is the scan speed (mm/s), h is the hatch spacing (mm) and t is the layer thickness (mm). Energy density is a useful term since it combines several key parameters to describe the amount of energy imparted by the laser on to the powder bed at a point, and the same energy density can be reached using different combinations of these parameters. An adequate energy density is required for the full melting of powder to avoid largescale porosity; densities of up to 99.9 % have been achieved for correctly optimised energy densities [6,7]. Zhang et al. [8] undertook an extensive review of the relative structural densities of various energy density values and found that an energy density as low as 41 J/mm^3 is capable of producing an LPBF SS316L component of 99 % density. Ponticelli et al. [9] found that increasing volumetric energy density can lower the resulting fatigue limit of LPBF SS316L samples, where they estimated that the average fatigue limit of vertical (90°), diagonal (45°) and horizontally (0°) built samples was approximately 131 MPa at 35.02 J/mm^3 compared to 119 MPa at 40.90 J/mm^3.

Despite the potential of creating a fully dense structure to improve fatigue resistance, there are several drawbacks that need consideration when continually increasing energy density. For instance, a balance needs to be sought in order to achieve a final material consisting of minimal defects or microstructural texture. A lack of suitable fusion will leave large cavities within the microstructure, whereas excessive heating is a cause of keyhole porosity and deformation from residual stress [6,10]. Furthermore, increasing energy density beyond a certain point has been shown to have no benefit in reducing porosity of SS316L components [6] and can actually lead to an increase in porosity through the vaporisation of metal by the laser [11]. Likewise, a high energy density can also increase the build time and the related cost that this incurs. Therefore, there are still some challenges associated with the process, especially connected to the low production rates. Sun et al. [12] demonstrated that the build rate could be improved (by up to 72 %) by altering the laser power and scan speed while maintaining a high density. However, there is minimal research detailing how different processing parameters affect the characteristics of the microstructure. A review of process parameter selection for LPBF SS316L was conducted by Ahmed et al. [11] where a dozen sources were identified that had achieved densities over 99 % with optimised LPBF manufacture. The energy density used to achieve this varied significantly between studies (53 J/mm^3–174 J/mm^3) as did powder layer thickness (20 μm–250 μm). However, the variation in process parameters for fully densified material shows the need to fully optimise individual processes and maintain stringent tolerances in process parameters for the LPBF of SS316L. The part's size and shape are other factors that can influence what the optimised set of process parameters is [13,14]. The shape and size of the part influence the thermal history experienced during the AM process, which can ultimately affect the porosity.

Several publications have reported the role of processing parameters on the resulting mechanical performance of LPBF SS316L [6 15 16 17 18] but relatively few studies have investigated the dynamic response of LPBF SS316L components, particularly under imposed strain low cycle fatigue (LCF) conditions. One of the main concerns when assessing the fatigue properties of AM materials is the presence of process-induced defects, such as those related to a lack of fusion (LoF), keyholing,

solidification cracking and the inherently rough as-built surfaces. Reimer et al. [19] found that the high cycle fatigue (HCF) performance and crack growth behaviour of LPBF SS316L are not significantly influenced by process induced imperfections, such as pores and internal stresses. However, Beard et al. [20], who undertook an extensive study on the role of surface finish on the LCF behaviour of LPBF SS316L found that surface roughness was the key parameter influencing the cyclic properties in the low cycle regime, and this was more pronounced in diagonally built samples with an as-built surface finish as opposed to vertically oriented samples, due to partially melted powder particles at the surface and the staircasing effect. This in turn led to a larger effective stress concentration factor at the surface, and a reduction in the resulting fatigue life. This effect was compounded by the underlying anisotropy in the contrasting microstructures where the vertically built LPBF material was shown to exhibit a superior strain-life response. Yet, in both instances, the LPBF material significantly outperformed the conventionally manufactured wrought equivalent.

Avanzini [21], Shrestha et al. [22] and Ponticelli et al. [9] all found that anisotropy plays a key role in the fatigue response of LPBF SS316L, where horizontal samples exhibited the highest fatigue resistance among the three principal build orientations (vertical, diagonal, horizontal) in all three studies. The study by Ponticelli et al. utilised reversed bending to exert a cyclic load on the samples and found that the superior fatigue properties in the horizontal material could be attributed to the orientation of the deposited layers with respect to the applied load, which for the horizontally built samples was perpendicular to the stress induced by bending, thus making a more tortuous crack path. Zhang et al. [8] found that HCF crack initiation is more sensitive to slip planes in dendrite cells or grain boundary particles as opposed to subsurface defects such as gas porosity. Likewise, by manipulating the process parameters and ensuring an increase in the cooling rate during solidification, for example by lowering laser power, this can improve fatigue resistance by promoting intergranular fatigue crack initiation and crack branching. In contrast, in the studies by Liang et al. [23] and Shrestha et al. [22], sub-surface defects such as LoF were found to be the dominant factor influencing the fatigue properties of LPBF SS316L. However, Liang et al. reported that the LoF features were populated in clusters and became more pronounced if located in close proximity to the surface, whilst the material in the report by Shrestha contained a significant number of larger LoF defects in the order of > 100 μm.

Despite the findings detailed previously, there is still a lack of knowledge as to how the parameters of the LPBF process can be optimised to improve the productivity of LPBF SS316L components, whilst not comprising on the material's favourable cyclic properties. This study investigates the influence of energy density on the structural density and surface roughness of LPBF SS316L samples built in the three principal build orientations, and the effect that these factors have on the low cycle fatigue behaviour of the alloy under strain control conditions.

2. Experimental methods

2.1. Material and samples

For this study, two batches of LPBF SS316L samples were manufactured on alternative additive manufacturing systems. The first batch were manufactured using an EOS M290 machine in a nitrogen atmosphere with powder supplied from LSN Diffusion. The second batch were fabricated using a Renishaw AM 250 machine in an argon atmosphere with powder sourced from Carpenter Additive. The composition of each powder batch is displayed in Table 1. Prior to sample manufacture, both powder batches were sieved to ensure uniformity and analysis of the powder showed particle size distributions of 5–60 μm (for the first batch) and 15–53 μm (for the second batch).

For the samples manufactured in the first batch, standard manufacturer recommended process conditions for SS316L were used, as defined by EOS, with a layer thickness of 20 μm and a volumetric energy density of 100.03 J/mm^3. For the purposes of this research, these samples are now referred to as high energy density (HED). For the samples manufactured as part of the second batch (on a Renishaw AM 250 with powder provided from Carpenter Additive), the process parameters included a laser power of 200 W, laser scan speed of 667 mm/s, hatch distance of 110 μm and a layer thickness of 50 μm. These build parameters combined for a volumetric energy density of 54.5 J/mm^3, approximately half the value used for the samples manufactured in the first batch, and an overall faster manufacturing process. These samples are now recognised as low energy density (LED) samples.

Table 1
Nominal composition of SS316LN powder batches manufactured by gas atomisation.

Element	LSN Diffusion (wt%)	Carpenter Additive (wt%)	Element	LSN Diffusion (wt%)	Carpenter Additive (wt%)
Al	0.005	–	N	0.005	–
B	0.001	–	Nb	<0.010	–
C	0.010	0.024	Ni	12.420	0.09
Co	0.020	–	O	0.010	0.02
Co + Ta	0.020	–	Ph	–	0.004
Cr	17.040	17.57	S	0.014	0.008
Cu	0.010	0.03	Si	0.350	0.65
Fe	Balance	Balance	Ti	<0.005	–
Mn	1.200	2.3	V	<0.010	–
Mo	2.530	12.52			

In each batch, two sets of samples were manufactured. One set of samples were fabricated to net-shape to enable a characterisation of the as-built surface, whilst the others were in the form of cylindrical or octagonal rods that were subsequently machined into LCF samples containing a longitudinally polished surface, with a surface roughness below 0.2 μm in accordance to [24]. Fig. 1 presents the base plate designs used for the two sample batches and Table 2 presents the number of samples manufactured for each type of sample for the purposes of this research.

In both sample batches, for the manufacture of diagonally built 45° angled samples, support structures were required. The supported region was located on the upper radius section, from the gauge length diameter to the maximum sample diameter, and was machined away prior to testing and polishing. No samples failed in this machined surface region that is situated outside of the parallel gauge length and is therefore considered to have negligible effect on the testing results.

Prior to sample manufacture, all of the cylindrical/octagonal rods and net-shape samples were removed from the respective base plates using wire EDM and were subjected to a hot isostatic pressing (HIP) procedure in order to consolidate the material [25]. The HIP cycle consisted of a heat treatment above the SS316L solution temperature and was held at this temperature for 2 to 3 h prior to cooling. The strain controlled LCF samples were machined according to the dimensions depicted in Fig. 2.

2.2. Low cycle fatigue testing

LCF tests were performed according to ASTM E606 [24] using a servo-hydraulic mechanical test machine and were tested at 20 °C under controlled laboratory conditions. All tests were carried out using a 0.004 s^{-1} triangular waveform and a fully reversed, R value of −1. To provide a range of strain-life data, several applied strain amplitude (ε_a) values were employed, namely 0.0018, 0.002, 0.003, 0.006 and 0.008 mm/mm. The number of fatigue cycles to failure (N_f) is reported as a 25 % drop from the peak load at the stabilised condition (as determined through linear regression). All samples were tested until failure or once 100,000 fatigue cycles were surpassed, upon which the test was stopped, the sample was unloaded, and the test was deemed a run-out.

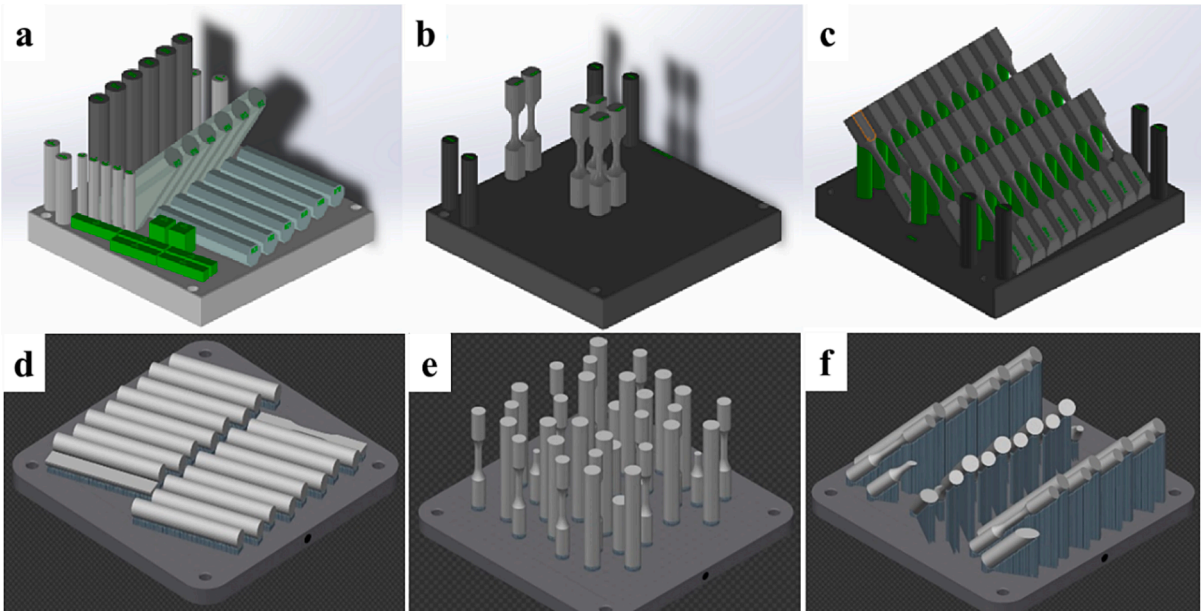

Fig. 1. Build plate designs for HED and LED LPBF samples a) HED cylindrical and octagonal rods, b) HED net-shape vertical (90°) samples, c) HED net-shape diagonal (45°) samples, d) LED horizontal (0°) cylindrical rods, e) LED net-shape vertical (90°) samples and f) LED cylindrical rods and net-shape diagonal (45°) samples.

Table 2
List of LPBF SS316L samples manufactured under HED and LED LPBF conditions.

HED LPBF Samples				LED LPBF Samples			
Orientation (°)	**Sample Type**	**Surface Finish**	**Number**	**Orientation (°)**	**Sample Type**	**Surface Finish**	**Number**
90	Net-shape	As-built	6	90	Net-shape	As-built	7
90	Cylinder	Polished	5	45	Net-shape	As-built	8
45	Net-shape	As-built	12	45	Cylinder	Polished	7
45	Cylinder	Polished	5	0	Cylinder	Polished	4
0	Octagonal	Polished	17				

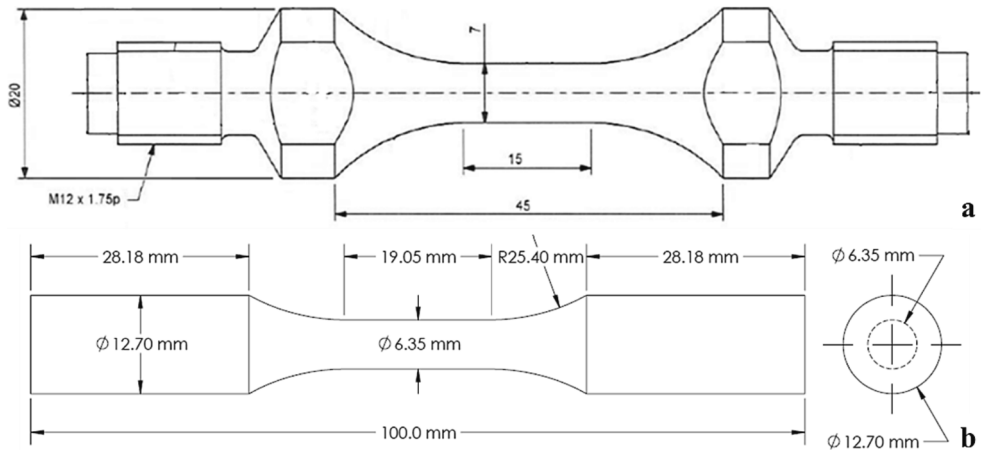

Fig. 2. Sample geometry for LCF testing a) HED samples and b) LED samples.

2.3. Surface roughness measurements

Prior to testing, an Alicona Infinite Focus microscope was used to measure the roughness topography and the interrelated parameters of samples from each sample type, according to ISO 21920-3:2021 [26]. Some of the typical parameters measured include R_a (average roughness profile), R_t (total height of roughness profile), R_p (maximum profile peak height), R_v (maximum depth of the profile below the mean line within the sampling length) and R_z (the average values of the heights of five highest-profile peaks and the depths of five deepest valleys within the sampling length). The full definition of the different surface roughness parameter types and those recorded are given in [20].

2.4. Microscopy, defect and fractographic analysis

A Hitachi SU3500 SEM, with electron backscatter diffraction (EBSD)

capability, was used to inspect the microstructures and the fracture surfaces of the different sample types. For EBSD analysis, scans were acquired using a step size of 1.5 μm and 4 × 4 binning. The phases chosen for acquisition were FCC-Fe and BCC-Fe, with the band detection mode optimised for EBSD. EBSD data was analysed using the Tango plug-in included in the Channel 5 software. Grain detection was performed using the grain area determination in Tango software, where no border or corner grains were included. Grain size of the X-Y and X-Z face of each sample type was measured by Channel 5 software.

A Zeiss Smartzoom 5 optical microscope was used to analyse the defect population of a selection of the different LPBF SS316L variants. Samples were prepared using standard metallographic procedures, and were then subjected to vibratory polishing on a VibroMet 2 polisher with OP-S (colloidal silica suspension) for ~ 8 h to remove remaining minor-deformations.

3. Results & discussion

3.1. Material

3.1.1. Microstructure

The microstructures of the different LPBF SS316L variants are displayed in Figs. 3 and 4 for each respective material batch. The main difference between the HED and LED material is the apparent lack of texture and anisotropy present in the LED material (Fig. 4). This is in stark contrast to the HED material which appears to be highly textured within the ⟨101⟩ direction, parallel to the build direction (Z-direction), as evidenced in Fig. 3a. Such texture is typical of LPBF SS316L [19], but depending on the scanning strategy, such a strong crystallographic texture is sometimes not present, or can be manipulated by modifying the laser power and hatch spacing. This corresponds to the morphology of the LED samples, which exhibit a lack of texture that is likely a result of the lower energy density utilised during manufacture. The relationship between ⟨101⟩ texture and energy density for LPBF SS316L was previously explored by Leicht et al. [6], who found that ⟨101⟩ texture decreased by 4 times when energy density was decreased from around 200 J/mm^3 to 50 J/mm^3. Their results also mirrored the same change in texture to the HED and LED samples described here, when using the same energy densities of approximately 100 J/mm^3 and 50 J/mm^3, respectively. The greater energy density leads to greater directional cooling which promotes the ⟨101⟩ texture. There is a small presence of high angle grain boundaries (the majority of which can be observed between 30 and 60°) remaining in the respective structures and misorientation can be seen to still be present inside several larger grains, which suggests that full recrystallisation has not occurred.

The EBSD scans of the different material types were used to calculate microstructural measurements including average grain size and grain aspect ratio, as given in Table 3. The measurements show that in general, the LED samples exhibit a more refined grain size with a higher aspect ratio, indicating that the grain morphology predominantly consists of

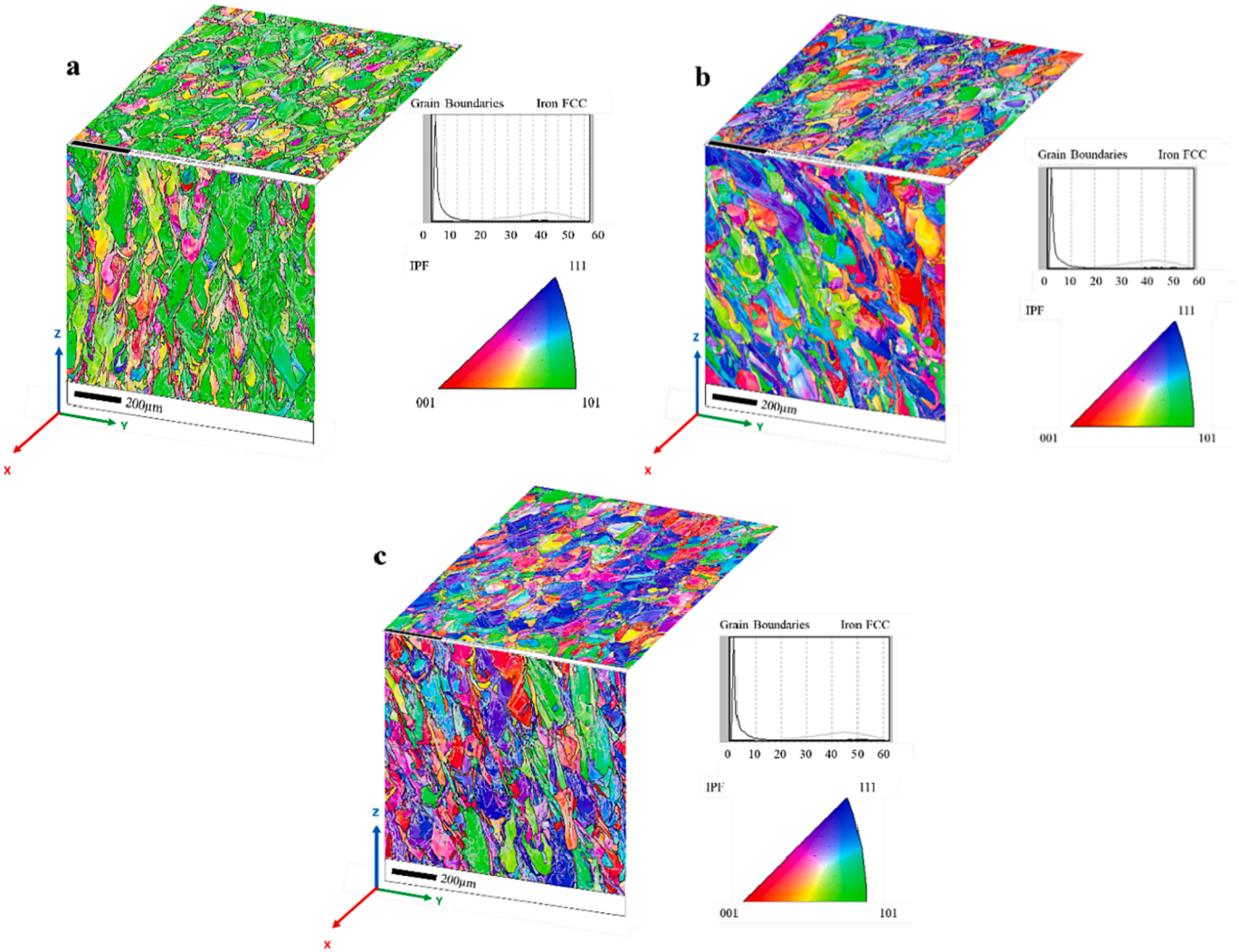

Fig. 3. Inverse pole figure (IPF) maps of HED LPBF SS316L samples a) 90°, b) 45° and c) 0°.

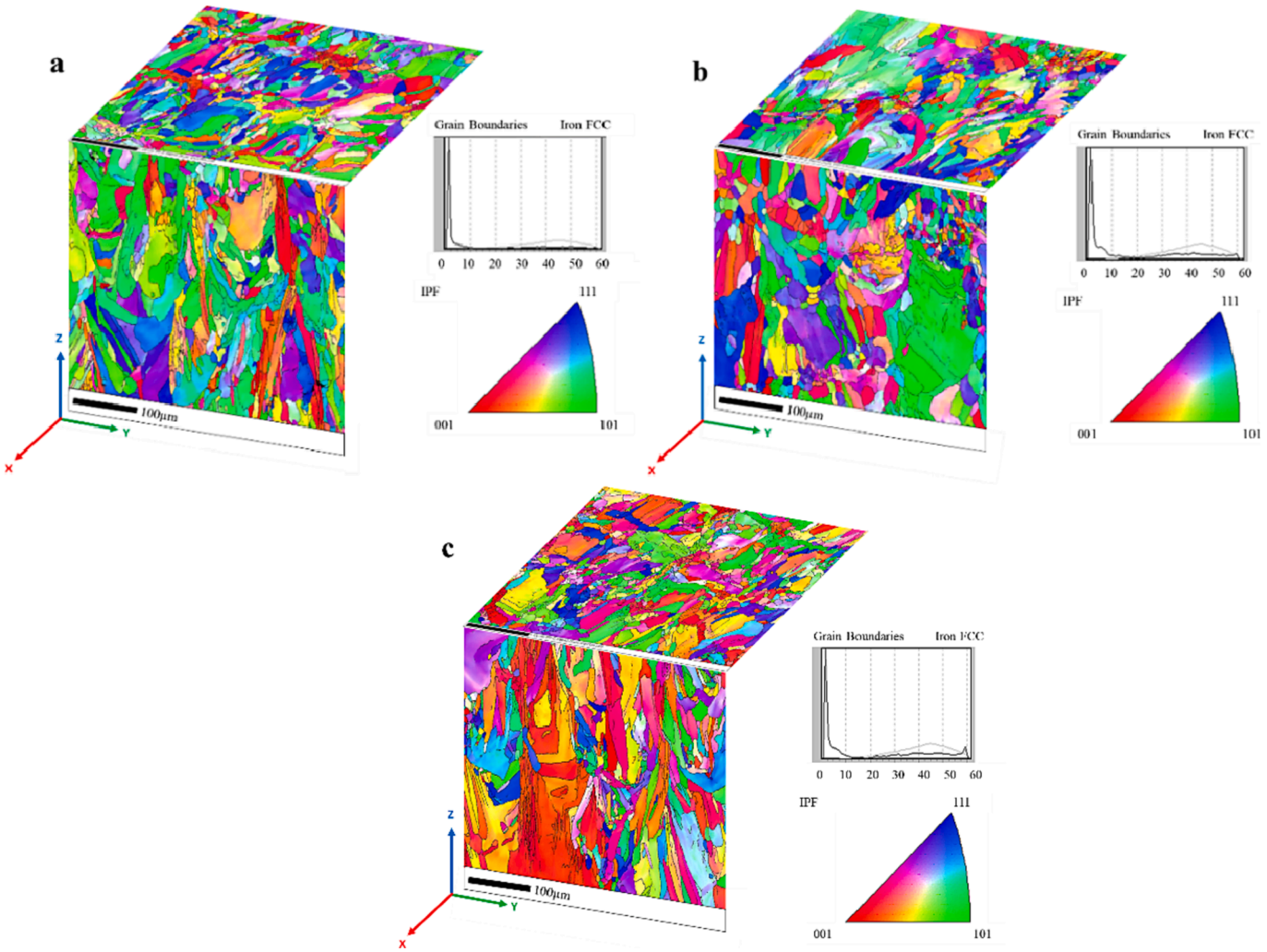

Fig. 4. Inverse pole figure (IPF) maps of LED LPBF SS316L samples a) 90°, b) 45° and c) 0°.

Table 3
Average grain size measurements for LPBF SS316L variants including aspect ratio and quantity of BCC phase present.

Batch	Sample	Average Grain Size (μm^2)	Aspect Ratio	Amount of BCC phase (%)
HED	90° X-Z	340	0.37	0.2
HED	90° X-Y	176	0.49	0.4
HED	45° X-Z	200	0.47	0.5
HED	45° X-Y	255	0.41	0.2
HED	0° X-Z	300	0.37	0.5
HED	0° X-Y	151	0.48	0.3
LED	90° X-Z	221	0.43	1.2
LED	90° X-Y	121	0.53	0.9
LED	45° X-Z	209	0.54	0.4
LED	45° X-Y	177	0.56	0.5
LED	0° X-Z	243	0.43	0.6
LED	0° X-Y	142	0.56	0.6

smaller equiaxed grains. However, for LED samples built in each of the three orientations, the aspect ratio of the grains on the X-Y plane are higher than those on the X-Z plane. This is to be as expected, given that the X-Z plane captures the epitaxial build orientation resulting from the LPBF process, but also reveals a slight level of anisotropy in these structures. Other factors to note here are the almost fully austenitic structures across all sample types for both energy densities, with very little indication of any solid-state phase transformations and only a minute presence of retained Body Centre Cubic (BCC) δ-ferrite (<1.2 %).

3.1.2. *Defect population*

Fig. 5 illustrates a typical example of the significant presence of porosity within a LED 45° sample in both the X-Y and X-Z plane, with the equivalent planes of the HED 45° sample presented in Fig. 6. In each figure, the images were captured on polished unetched surfaces, yet the final stage of the polishing procedure using OPS suspension has partially etched the surface revealing some microstructural detail. At their largest, the porosity features are in excess of 600 μm in diameter and often contain smaller particles within them, in spite of the post-manufacture HIP operation. Most of these particles are smaller spherical features with a range of diameters, but the majority fall within a 20–50 μm range. This corresponds well to the powder size distribution, and larger spherical objects are anticipated as being agglomerations of partially fused powder particles. These unfused powder particles often appear either very weakly attached or not attached at all to the rest of the material in the image. Many pores don't appear to contain any loose powder particles and it could be that during material preparation, the loose powder that was within these pores has fallen out. The pores are typical of LoF defects as reported by other researchers [27,28].

The defect population in the LED material is in stark contrast to the behaviour in the HED counterpart. Fig. 6 presents the images captured of a HED 0° sample and shows that the material appears to be almost fully dense. Apart from a few isolated features, the HED material offers a density of > 99 %. This difference is despite both sample types being

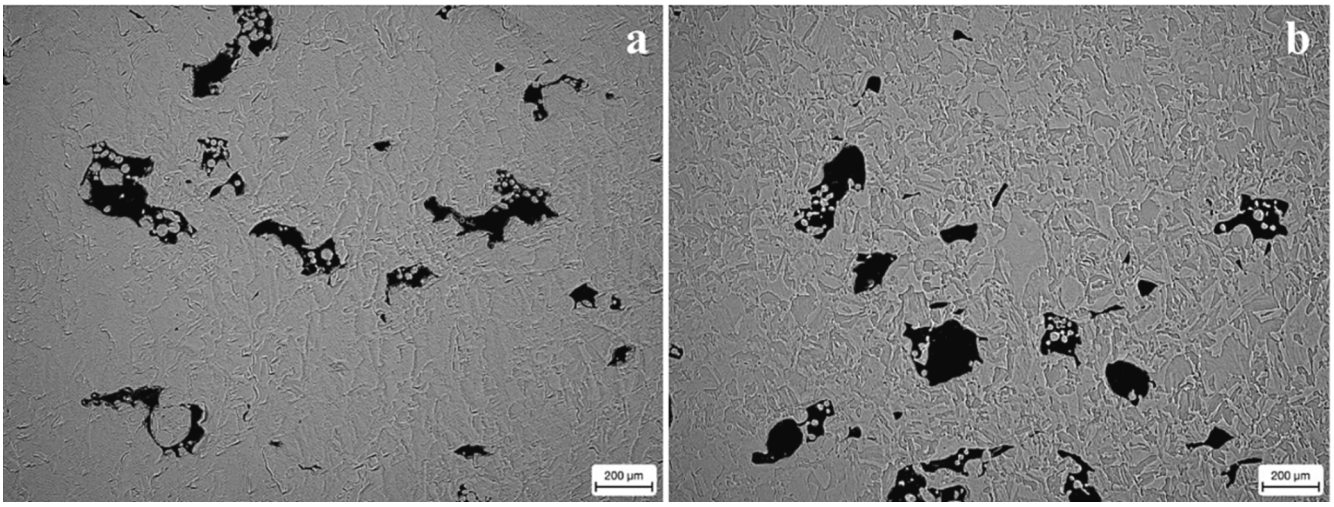

Fig. 5. Porosity content in a LED 45° sample a) X-Y plane, b) X-Z plane.

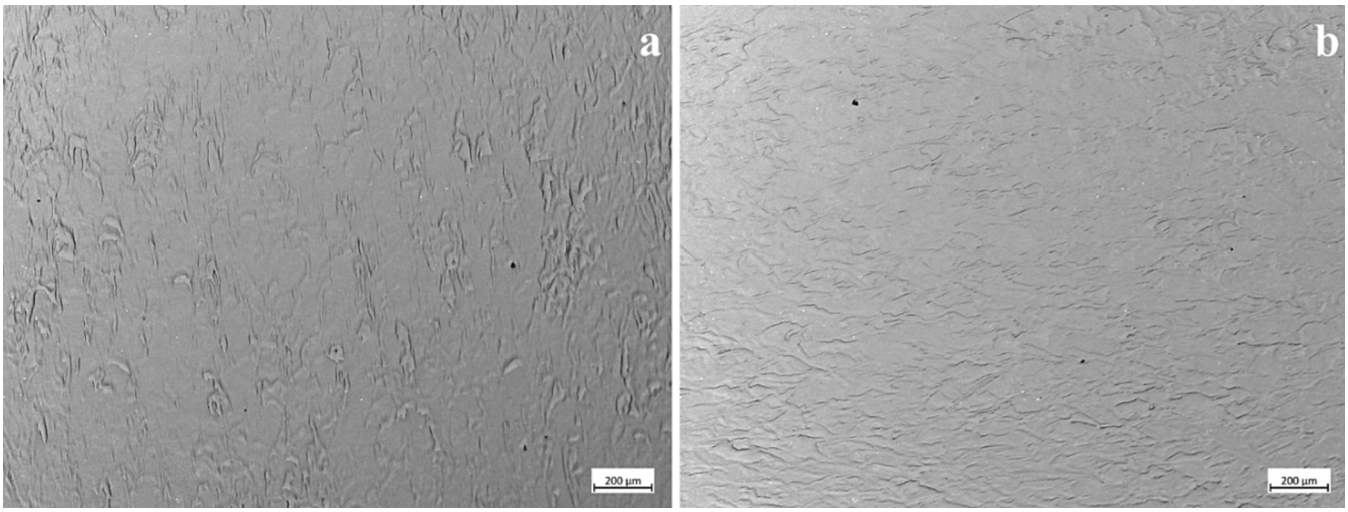

Fig. 6. Porosity content in a HED 0° sample a) X-Y plane, b) X-Z plane.

subjected to the same post-manufacture HIP operation. HIP is a commonly used post-manufacture procedure that involves placing a metallic component within a vessel that is pressurised and heated [29]. Argon pressurisation exacts an isostatic force equally around the whole part to densify it and can also be used to create parts from compacted powder [30]. Previously, post-manufacture HIP operations have been used to densify approximately 90 % of pores within LPBF material [31]. In the study by Ruttert et al. [32], the average size of remaining pores was also significantly reduced. This densification along with the homogenisation of the microstructure via heat treatment in HIP can lead to improved fatigue lives, as well as a reduction in variation for samples built in different orientations. Elsewhere, HIP of as-built LPBF SS316L components reduced porosity volumes to below 1 %, where pores of up to 800 µm in diameter were observed to close up [33]. Yet despite the positive effect that HIP can have on improving the structural density, it can also induce some recrystallisation and also an element of grain growth since HIP processing is typically undertaken at an elevated temperature, often above the solution temperature of the material. As such, to optimise the material's resistance to cyclic loading, a careful balance is necessary to HIP under the correct conditions in order to reduce the amount of internal porosity but also limit the extent of grain growth.

The main discrepancy between the two material types can be related to the energy density used, but also the environment in which the samples were manufactured. While the LED samples were built within an inert argon chamber, the HED samples were manufactured in a nitrogen backfilled system. Typically, during the LPBF process, gas from the build chamber has the potential to be trapped. Trapped gas creates porosity throughout the material, the scale of which is determined by the optimisation of the build process. In this investigation, both sample types were subjected to a HIP operation post manufacture, in order to densify parts and create a more homogeneous structure. However, HIP is not as effective in material formed in an argon atmosphere since argon becomes trapped within the porosity sites. Valente et al. [34] previously documented that using argon during manufacture produced a more heterogeneous structure, as opposed to building with nitrogen. However, argon was also found to fill porosity defects and since it is not soluble within steel, the pores were unable to diffuse through the material during HIP treatments and were not completely removed, leading to only a partial improvement in the material's density. Instead, the argon filled porosity features become compressed [29]. Further heat treatment after this HIP process can result in the gas within the argon pores expanding and increasing the volume of porosity [35]. Whereas, using nitrogen in place of argon has been documented to lead to an increase in the weight percent of nitrogen within the as-built material resulting in increased material hardness [34 36] and lower porosity,

often resulting in longer fatigue lives in steel [37]. However, despite the presence of porosity, the reduced energy density in the LED samples promoted a finer grain microstructure, with a more uniform equiaxed morphology, less crystallographic texture and reduced anisotropy, all of which are desired when designing a material to resist cyclic deformation. However, all of these benefits are overcome by the significant presence of LoF defects which could not be fully eradicated during HIP.

It is also important to consider the layer thicknesses used in the manufacture of the two alternative sample batches. The LED samples were manufactured with a layer thickness of 50 μm as compared to 20 μm in the HED samples. The greater layer thickness would typically require the laser energy to be distributed over a greater volume for appropriate remelting between layers. It appears here that the energy of the laser used for the LED builds is not sufficient enough to melt a suitable thickness of powder to enable enough melting between adjacent layers. This behaviour was also previously reported by Hatami et al. [38] where it was found that a significantly higher porosity content in LPBF SS316L samples manufactured with a 50 μm layer thickness as opposed to those with a 30 μm layer thickness, which subsequently also had an effect on the resulting fatigue life. However, it should be noted that high densities can be achieved with thicker layers, providing that the energy density employed is high enough. Previously, Cherry et al. used a 50 μm layer thickness and an energy density of 104.52 J/mm^3 to achieve a porosity percentage of 0.38 % in LPBF SS316 [39]. Likewise, Sun et al. manufactured LPBF SS316L cubes with 12 different parameter sets but importantly, all with a layer thickness of 50 μm and an energy density between 98.70 and 108.57 J/mm^3 [12]. All these samples had a densification of greater than 99 %.

Quantitative analysis was performed on a selection of the different LED sample types, with the calculated values presented in Table 4. For each build orientation, the porosity contents of two examples are provided; one of which refers to the best performing sample under LCF conditions (#1), and the other where the sample appeared to fail prematurely (#2). For each sample, a total of 5 micrographs were analysed of each X-Y/X-Z plane to provide a suitable representation of the porosity volume fraction percentage. Also given in Table 4 are the corresponding minimum and maximum volume fraction percentages to provide an indication of the scatter.

As can be seen in sample #2 for each build, on each plane of each respective build orientation there is a considerable presence of porosity. Of the three different build orientations, the LED 0° build appears to have the least dense structure (<97 %), with porosity features exhibiting a larger morphology on the X-Y face compared to the X-Z plane. The opposite behaviour is seen in the LED 90° build, where the LoF defects have a larger dimension on the X-Z plane. This relates to the nature of the LoF defects between adjoining melt layers and their orientation in regards to the build direction. Such morphologies can play an important role in influencing the resulting fatigue performance of the LPBF variants. However, even though the values provide an indicative representation of the severity of defects in the LED samples, it is difficult to ascertain the precise volume fraction of defects without the use of X-ray computed tomography (XCT) due to the non-uniform distribution of defects within the structures. Therefore, the values here provide a tentative quantification of the level of porosity found in a selection of samples, but these percentages can be assumed to be a 'best-case' examples, since more porous regions are possible in each material. The materials selected for samples labelled #1, refer to those that best performed under LCF conditions, where a more optimal structural density is envisaged. As can be seen, these samples exhibit structural density values comparable with the HED samples (>99 %). Therefore, given the large range of scatter seen in the porosity volume fractions in the LED variants, it would be expected that the resulting fatigue performance would suffer from a similar variation. To clarify, the porosity content of a selection of the HED samples was also measured, but all planes for each build orientation were found to have < 1 % porosity. As such, they were deemed to be fully, or > 99 %, dense.

Table 4
Average porosity volume fraction percentages for LPBF SS316LN samples. The bracketed values represent the minimum and maximum volume fraction percentages recorded from 5 micrographs for each plane/sample.

Sample	Porosity X-Y	Porosity X-Z
LED 90° #1	0.01% (0.01–0.02%)	0.01% (0.01–0.02%)
LED 90° #2	3.73% (0.01–5.91%)	3.80% (0.05–4.89%)
LED 45° #1	0.02% (0.01–0.03%)	0.02% (0.01–0.02%)
LED 45° #2	2.71% (1.07–4.58%)	3.48% (1.80–4.82%)
LED 0° #1	0.01% (0.01–0.02%)	0.03% (0.01–0.05%)
LED 0° #2	4.28% (1.41–6.26%)	3.12% (0.26–6.28%)

3.1.3. Surface roughness

Surface roughness measurements were recorded on a selection of LED and HED as-built and longitudinally polished samples. All polished samples were prepared to the same surface roughness where the polishing procedure involved the removal of surface material to a maximum roughness value so that surface roughness effects from varying orientations were removed. The surface roughness parameters for a selection of the different LPBF SS316L samples are presented in Table 5. In the as-built samples for both the LED and HED materials, it is noticeable that the 45° angled samples have a rougher surface finish compared to the 90° equivalents (HED 90° R_a = 14.42 μm, HED 45° R_a = 22.06 μm, LED 90° R_a = 8.847 μm, LED 45° R_a = 23.885 μm). Similarly, this behaviour was seen in regards to the maximum peak to valley height (R_t), where in both the HED and LED samples the R_t value of the 45° samples was twice that of the 90°. This behaviour was also the case for maximum peak height (R_p), maximum valley height (R_v) and mean peak to valley height of the roughness profile (R_z). As reported previously [20], the extra roughness in the 45° orientated samples originates from the staircase affect when manufacturing AM components. As parts are manufactured in single layers, an overhanging surface needs to be manufactured with slightly overlapping layers in a staircase design, which increases surface roughness [40]. In addition to this, the downskin is particularly badly affected as less favourable heat conduction to the powder bed below occurs as opposed to the top skin where heat can dissipate more quickly down through the part [41 42]. It is also important to consider the interaction between the melt pool, consolidated material and surrounding bed of powder. Beard et al. [20] previously discussed how for a vertically (90°) built component, half of the melt pool is exposed to unmelted powder that is not subsequently melted during manufacture. This loose powder at the surface that remains in contact with the melt pool only partially melts and results in multiple powder particles adhering to the surface, increasing the surface roughness. However, for the downskin on a 45° surface, the majority of the melt pool is exposed to loose powder, along with the base of the melt pool not being supported by consolidated material. This allows the melt pool to sink into the loose powder bed below, subsequently increasing in size and partially melting a large number of powder particles. This in turn results in surface breaking features greater than the size of a single powder particle or layer thickness and a significantly higher surface roughness as compared to 90° builds. Therefore, the 45° angled samples with an as-built surface finish would be expected to have an inferior resistance to fatigue deformation compared to those built at 90°.

In comparison, the longitudinally polished samples have a much

Table 5
Surface roughness parameters for LPBF SS316L samples.

Sample	R_a (μm)	R_t (μm)	R_p (μm)	R_v (μm)	R_z (μm)
HED 90° AB	14.42	74.27	40.71	33.58	39.37
HED 45° AB	22.06	128.34	57.68	70.66	83.65
LED 90° AB	8.85	83.43	38.13	45.30	59.91
LED 45° AB	23.89	163.17	90.99	72.22	116.46
LED 0° P	0.91	7.72	4.16	3.55	6.50

lower surface roughness and the surface roughness parameters are quite similar across the different energy density and build orientations, as would be expected given the consistency of the polishing procedure. Elangeswaren et al. also reported that surface polishing to remove stress raising features on the surface, such as unfused powder, greatly improved fatigue life [43].

When directly comparing the as-built surface roughness across the two energy densities, the 90° LED samples appear to have a lower surface roughness (R_a = 8.847 μm) than the HED samples (R_a = 14.42 μm) whist the as-built finishes for the 45° angled samples are comparable (LED R_a = 23.885 μm, HED R_a = 22.06 μm). However, in regards to maximum peak to valley height, for the 45° samples, the difference is much greater (LED R_t = 163.173 μm, HED R_t = 128.34 μm).

When comparing the surface roughness profiles of alternative build orientations and finishes, it is also important to consider the effective stress concentration factors (K_t) that roughness parameters induce. Pegues et al. [44 45] adopted the following relationship to calculate effective K_t values using several surface roughness parameters:

$$K_t = 1 + n\left(\frac{R_a}{\rho_{10}}\right)\left(\frac{R_t}{R_z}\right) \quad (2)$$

where n represents the changes in stress state ($n = 1$ for shear and $n = 2$ for tension), and ρ_{10} refers to the 10-point valley radii, which is estimated as the average radius of a micro-notch at the surface. As was the case in previous research by the authors [20], the assumption is that the as-built surface roughness is comprised of partially melted powder particles, and as such, micro-notches at the surface can be assumed to be dictated by these particles. Based on this, the ρ_{10} value was approximated as the radius of the powder size for the two powder batch types, namely 17 μm for LED and 14.5 μm for HED samples, respectively, for the purpose of quantifying the as-built surface roughness with an effective stress concentration factor. Using these values, the effective K_t values for the polished surface finishes ranged from 1.04 to 1.15, as would be expected given the repeatability and consistency of the polishing technique, which suggests the surface is free of any discontinuities. However, for the samples where the surface remained in the as-built condition, there is a considerable difference between the LED and HED sample types. In the 90° samples, the LED samples exhibited an effective K_t value of 2.45, whereas the same value for the HED samples was 4.75, approximately a factor of 2 greater. This difference would indicate that the LED samples would be expected to have a longer initiation life compared to the HED material. However, when considering the total fatigue life of a given material, which also encompasses the life during crack propagation, the greater presence of internal LoF defects also needs to be accounted for as it is likely that this will play a major role as cracking progresses through the material. In terms of the 45° samples, again there is a difference in the stress concentration values, where for the LED samples, the effective K_t was 4.94, and for the HED samples, the value was 5.67, again indicating the more severe stress raising features at the surface in the HED samples, and the rougher as-built surface finish of the 45° builds compared to the 90° samples. These values are summarised in Table 6.

3.2. Low cycle fatigue (LCF) results

Figs. 7, 9 and 11 present the LCF results from strain control tests on the various LPBF SS316L samples. Fig. 7 shows the strain-life plot and stabilised stress range response of the vertically built samples and have revealed the contrasting performances between the LED and HED samples. The HED samples can be seen to outperform the LED counterparts in both instances, with the polished material exhibiting the superior fatigue behaviour, followed by the HED as-built surface finish, and finally the LED material with the as-built finish, a behaviour similar to that seen in the review paper compiled by Avanzini [21]. Whereas the HED samples also offer a high level of consistency in the results, with well defined S-N data, the same can not be said of the LED samples. As discussed earlier, whilst the HED samples exhibit a more favourably fully dense structure as compared to the LED material, they also contain a larger grain size, greater magnitude of crystallographic texture and more severe stress concentration factors at the surface. However, the LED samples contain a significant presence of LoF defects and a much lower relative density. Therefore, whilst the LED material would be expected to have a comparable, if not superior, LCF response to the HED samples, the LoF defects have promoted a highly unpredictable fatigue behaviour, and this is reflected in the degree of scatter seen in the results, where two alternative data sets appear to co-exist. This discrepancy relates to samples that contain almost fully consolidated material, and those that do not. This can be seen in Fig. 7a, where a set of four data points sit quite favourably in comparison to the HED as-built finish samples, and three data points which are located far below the S-N data of the HED variants. This contrasting behaviour can be directly related to the defect populations seen in the different samples, where predictably, the samples that failed prematurely exhibit a relatively low structural density. Indeed, upon observing the materials' response on a stabilised stress range basis, the best performing LED as-built samples actually appear to outperform the HED counterparts. This can be seen more clearly in the hysteresis stress–strain loop response of the different 90° materials, as displayed in Fig. 8. In the first-cycle loops, the LED as-built sample reaches a higher yield stress than the HED as-built and polished samples, and also a higher maximum stress at peak strain. Yet, once peak stresses have stabilised, the maximum stress has cyclically softened by approximately 40 MPa, as is also the case for the HED as-built sample. However, the polished HED material exhibits the lowest degree of softening, maintaining similar maximum and minimum stress values for the duration of the LCF tests. This is reflected in the $\Delta\sigma$-N_f curve (Fig. 7b), where apart from the two tests that failed prematurely, the as-built samples lie on a similar curve, whilst the polished samples outperform both. The monotonic first-cycle loops also allow a comparison of the apparent Young's Modulus values and the difference between the three material types for this build orientation is minimal (HED polished = 193 GPa, HED as-built = 195 GPa, LED as-built = 196 GPa). In all cases, these values were calculated across a consistent stress interval of 0–200 MPa.

A similar behaviour is seen when considering the fatigue behaviour of the diagonally (45°) built SS316L samples. As given in Fig. 9, again the HED samples exhibit a more consistent behaviour as depicted by the clearly defined S-N response, whereas the LED material offers a large degree of scatter across both surface finish types. While on a ε_a-N_f basis, the best performing LED samples appear to have a highly comparable fatigue performance to the HED samples, on the $\Delta\sigma$-N_f curves, the contrasting data sets diverge more considerably, where a distinct difference in the cyclic behaviour is established. Here, the HED 45° polished samples exhibit the longest fatigue lives, followed by the HED as-built and LED polished samples which have a similar response, followed finally by the LED as-built material, where there is a clear knock-down in fatigue life. This can be potentially linked to the effects of the surface roughness. Whereas the effective stress concentration (K_t) for the as-built 90° HED sample was significantly higher than the LED

Table 6
Calculated effective K_t values for LPBF SS316L samples.

Sample	HED 90° P	HED 90° AB	HED 45° P	HED 45° AB	HED 0° P	LED 90° AB	LED 45° P	LED 45° AB	LED 0° P
Effective K_t	1.04	4.75	1.10	5.67	1.15	2.45	1.13	4.94	1.13

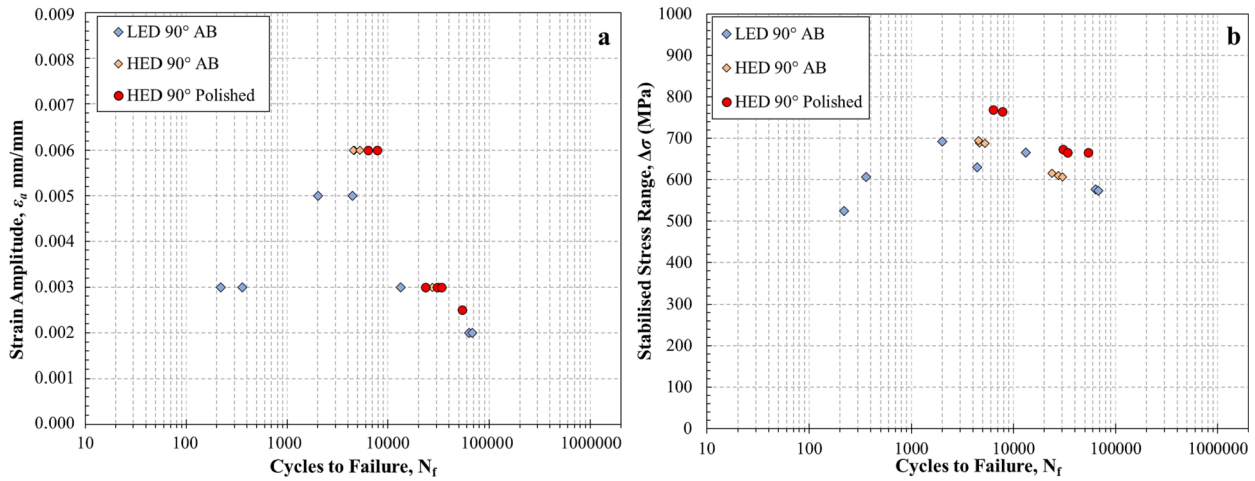

Fig. 7. LCF results for LPBF SS316L 90° LED and HED samples a) ε_{MAX}-N_f and b) $\Delta\sigma$-N_f.

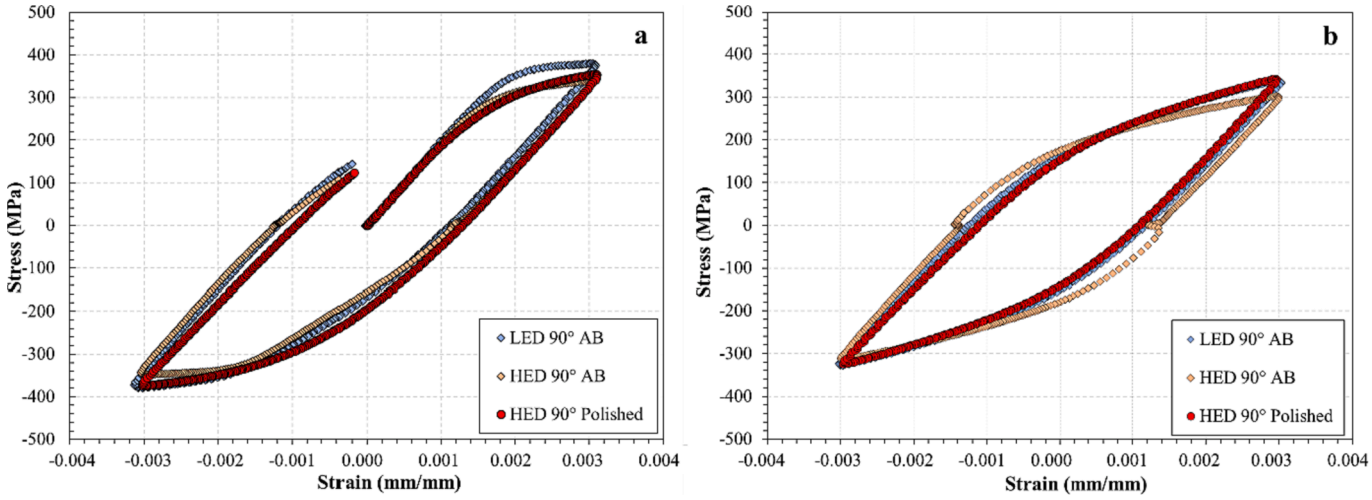

Fig. 8. A) first-cycle and b) stabilised strain–stress loop behaviour for LPBF SS316L 90° LED and HED samples, each tested at $\varepsilon_a = 0.003$ mm/mm.

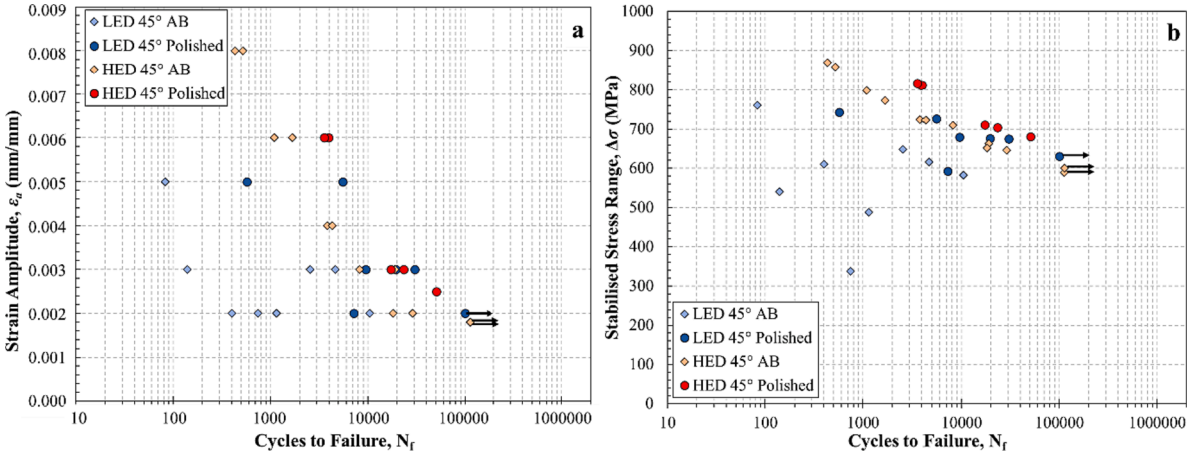

Fig. 9. LCF results for LPBF SS316L 45° LED and HED samples a) ε_{MAX}-N_f and b) $\Delta\sigma$ -N_f. Tests that run-out are indicated by an arrow.

equivalent ($K_t = 4.75$ compared to 2.45), for the 45° samples, the difference is far less significant. Given the marginal difference in the calculated K_t values, other factors become more significant, such as the presence of internal stress raising features including porosity sites and LoF defects.

The hysteresis stress–strain loop response of the different 45° angled samples is displayed in Fig. 10. Firstly, it can be noted that the different samples exhibit a range of apparent Young's Modulus values when measured from 0 to 200 MPa (HED polished = 193 GPa, HED as-built = 186 GPa, LED polished = 207 GPa, LED as-built = 184 GPa), with the

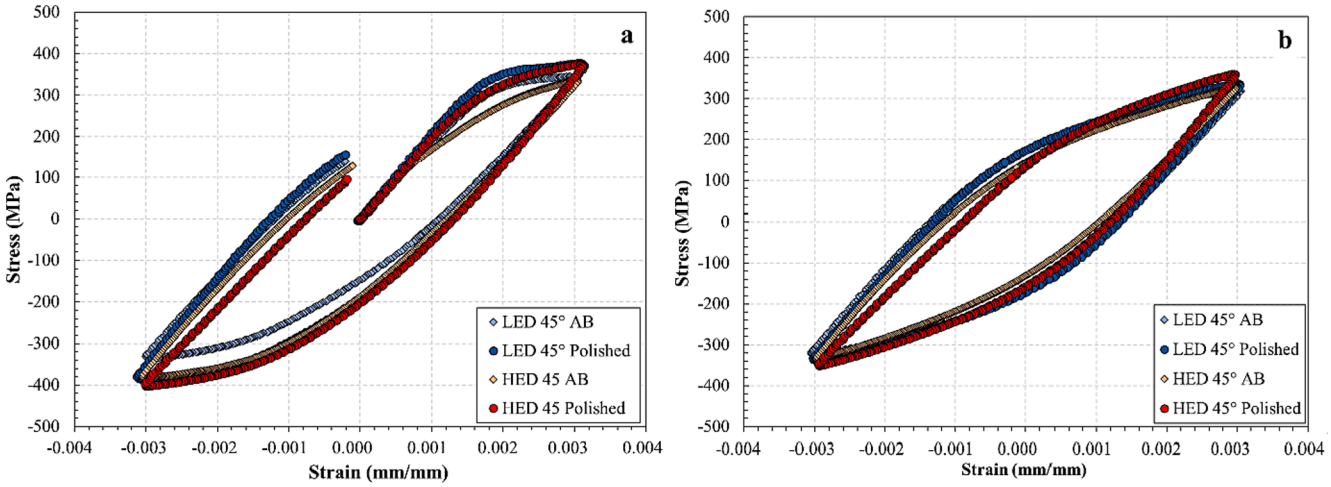

Fig. 10. A) first-cycle and b) stabilised strain–stress loop behaviour for LPBF SS316L 45° LED and HED samples, each tested at $\varepsilon_a = 0.003$ mm/mm.

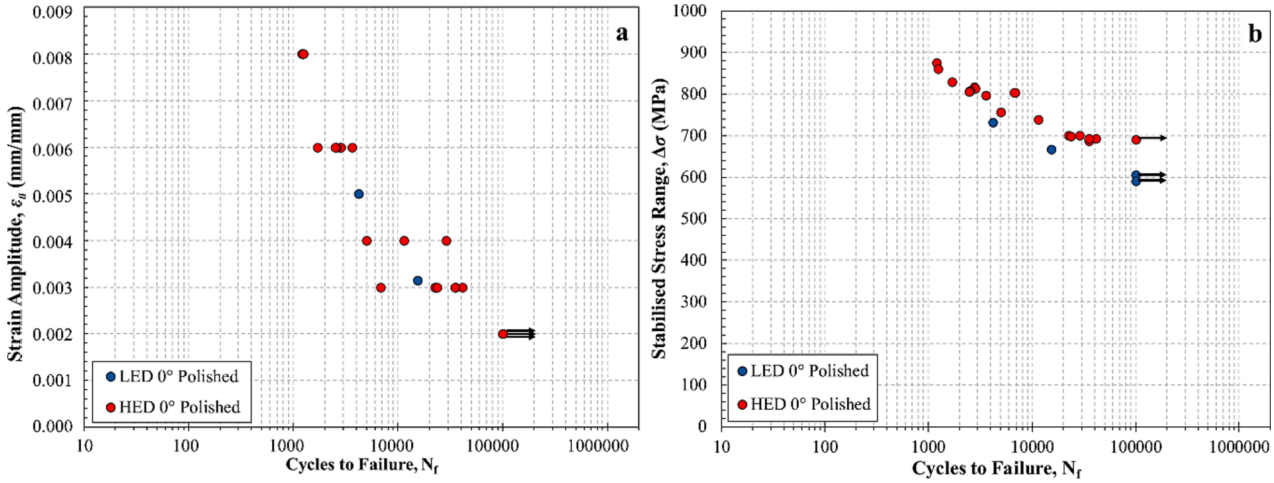

Fig. 11. LCF results for LPBF SS316L 0° LED and HED samples a) ε_{MAX}-N_f and b) $\Delta\sigma$-N_f. Tests that run-out are indicated by an arrow.

LED samples possessing a difference of more than 20 GPa when comparing the as-built to the polished equivalent. This difference is attributed to the random distribution of LoF defects in the LED samples, since porosity has previously been found to be highly influential on the Young's Modulus behaviour of L-PBF SS316L. In the study by Garlea et al., the apparent Young's Modulus of L-PBF SS316L was found to range from 140 GPa to 210 GPa, depending on the Archimedes density of the respective materials analysed [46].

The 45° as-built HED sample was also found to yield at a far lower stress value compared to the other variants, and this is due to this sample type exhibiting the highest effective stress concentrations at the surface and also a comparably larger grain size as compared to the LED material. The 45° material with the highest yield was the LED polished sample, yet once the material starts to plastically deform, there is very limited strain hardening as compared to the other material variants. This can also be seen in the stabilised loop condition, where the maximum stress of the polished LED sample has softened down to the same stress level as the as-built materials, whereas the polished HED sample is again capable of maintaining a higher magnitude of stress and softening the least. For each energy density, the polished samples typically outperform the samples remaining with an as-built finish. Of course, this can be related to the higher stress concentrations on an as-built surface, but also the reduced load bearing cross section that these sample types possess, and subsequently, a lower yield strength when compared to samples where the surface is more consolidated and uniform.

Finally, in the horizontally built samples, as displayed in Fig. 11, the S-N data for the polished LED and HED samples are highly comparable. This would be as expected, given the consistent surface finish across the energy density variants. Therefore, the differences between the two material types can be directly related to the presence of defects or the underlying grain morphology (Table 3). Given that the LED samples exhibit a finer grain size, they would be expected to have a stronger resistance to cyclic loading. As such, the main factor influencing the LCF behaviour of the LPBF SS316L 0° samples can be assumed to be associated with the defect population. This is surprising due to the minimal scatter seen in the LED samples. The hysteresis stress–strain loop behaviour of the horizontally built samples is depicted in Fig. 12, and it again shows the increased level of plasticity occurring in the LED samples, as the sample yields at a lower stress and is unable to reach the same maximum stress as the HED material. This occurs despite the two material types exhibiting the same apparent Young's Modulus of 193 GPa (when calculated between 0 and 200 MPa). It is important to note though that the LED sample was tested at a slightly higher ε_a value, yet the material does appear to yield at a lower stress, again likely due to the presence of the internal LoF defects. Vallejo et al. [47] previously documented that the yield and tensile strength properties of LPBF SS316L appeared to be more sensitive to the presence of LoF defects, as opposed to key hole porosity which tends to occur when an excessive laser power is employed. Despite this, in the stabilised condition the LED material is still capable of reaching a comparable maximum stress as the

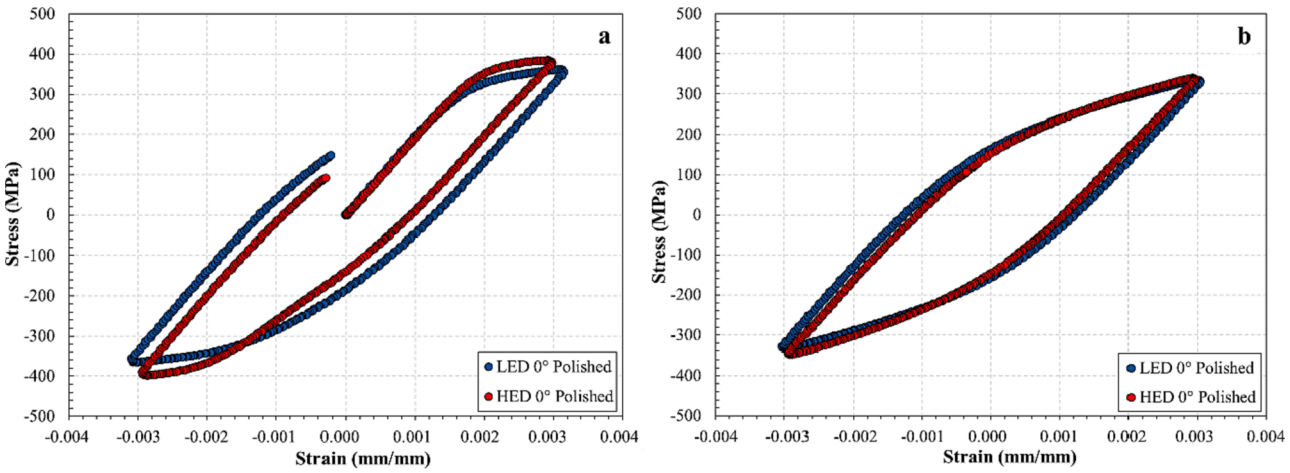

Fig. 12. A) first-cycle and b) stabilised strain–stress loop behaviour for LPBF SS316L 0° LED and HED samples, each tested at $\varepsilon_a = \sim 0.003$ mm/mm.

HED samples, whilst also cyclically softening the least of the two materials.

To corroborate the properties found from the hysteresis stress–strain loops presented in Figs. 8, 10 and 12 for the three different build orientations, a series of Vickers hardness indents were recorded on the X-Y and X-Z planes of each of the LED and HED variants. As expected, the hardness properties were consistent across the two energy densities, irrespective of the change of build orientation and plane. The LED and HED samples had average hardness values of 187 Hv_1 and 189 Hv_1 respectively. However, these values deviated when readings were recorded in the vicinity of lack of fusion defects, where the corresponding H_v value was significantly reduced.

When directly comparing the fatigue properties of the three different build orientations, it appears that there is little differentiation between the HED samples in the polished condition, particularly when considering the $\Delta\sigma$-N_f response. There is a slight ordering, whereby the

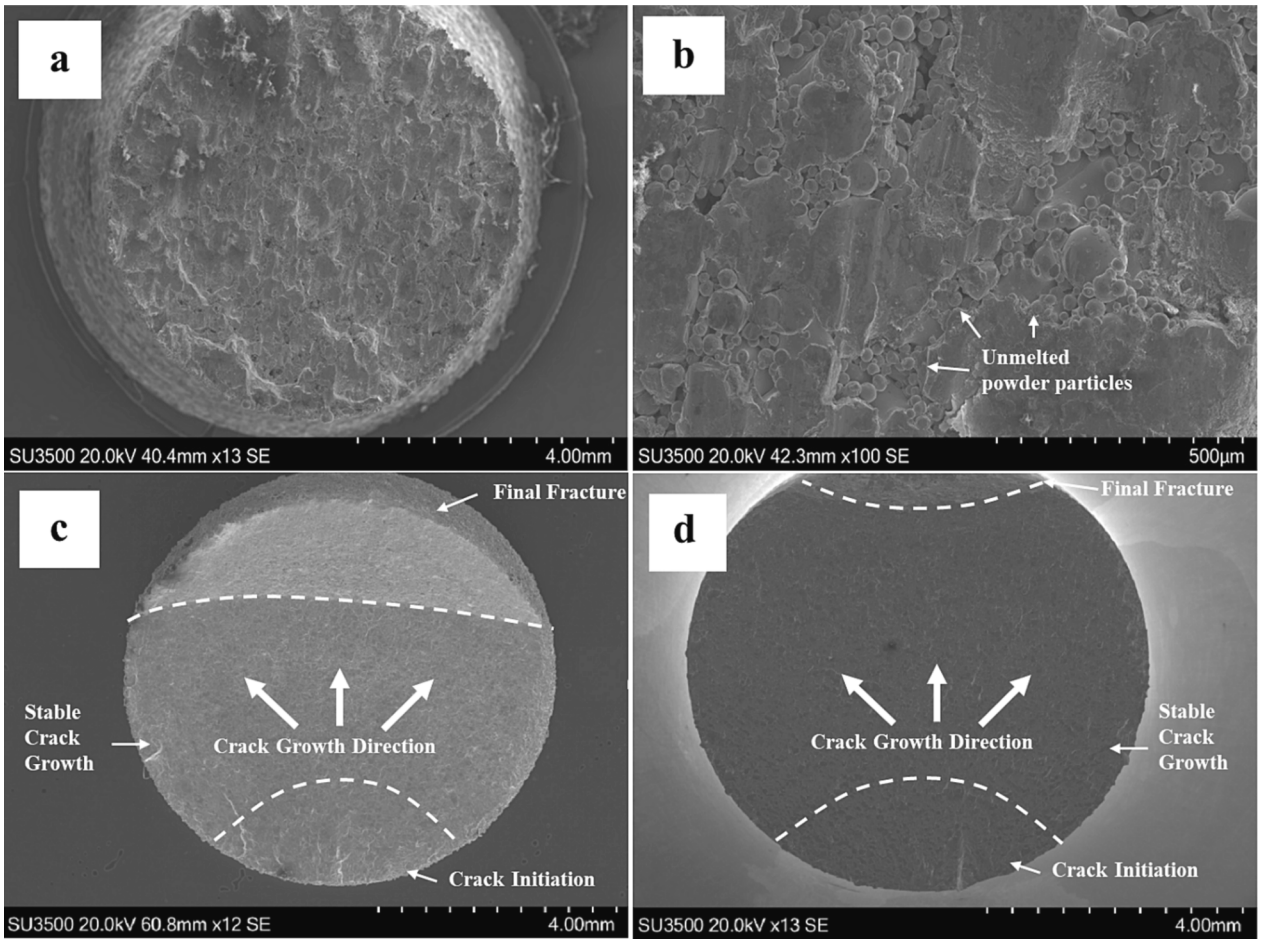

Fig. 13. SEM fracture surfaces of LPBF 90° SS316L LCF samples a) LED as-built, b) LED as-built (higher magnification), c) HED as-built, d) HED longitudinally polished.

0° samples generally exhibit the highest fatigue strength, followed by the 90° and finally 45° samples, a trend that coincides with previous work [22]. However, it is more difficult to directly compare the as-built equivalents due to the degree of scatter in the data that arises from the previously documented structural defects and the inherently rougher as-built surface finish. Shrestha et al. [22] also found that the effect of relatively smaller surface stress concentration features arising from the manufacturing process may not be as significant on the cyclic behaviour of the LPBF material as the presence of larger internal LoF defects.

The scatter observed in the LED samples also appears to be more pronounced at lower strain amplitudes ($\varepsilon_a = < 0.003$ mm/mm), where the level of plastic deformation under cyclic loading would be expected to be small, and therefore, the majority of the fatigue life will be dominated by crack initiation, which would be more sensitive to the presence of defects. Conversely, at higher strain values, the fatigue life would be expected to consist of a more significant portion of crack growth, which is less influenced by defective regions. Similar observations were found by Shrestha et al. [22], who also found that the presence of internal structural defects play a more significant role on the fatigue behaviour of LPBF SS316L material than anisotropic variations in the underlying microstructures, including the orientation of elongated grains, aspect ratio and grain size.

3.3. Fracture behaviour

Post test, a series of samples were subjected to fractographic investigations in order to understand the underlying failure mechanisms and whether any process induced defects or anomalies played a role in the deformation behaviour of the different LPBF SS316L samples. Fig. 13 presents a series of the typical fracture surfaces observed from the LCF tests on the 90° oriented LPBF samples and reveal significant differences relating to surface finish and energy density. The zone of crack nucleation is difficult to identify in the LED as-built sample due to the compressive nature of the loading cycle (Fig. 13a), but the surface is shown to have large porous areas containing significant quantities of unfused or very partially fused powder feedstock (Fig. 13b). The fatigue life of this sample fell to the left of the S-N data, effectively failing prematurely (after less than 500 cycles) compared to other 90° as-built LED samples tested under the same conditions ($\varepsilon_a = 0.003$ mm/mm) that reached more than 10,000 cycles. It can also be seen that crack growth is primarily transgranular, interacting with clusters of partially fused powder particles that are heavily populated on the surface. Such behaviour would also introduce a large element of scatter to the resulting fatigue life and this is reflected in Fig. 7. In contrast, the failure process of the HED samples resemble typical crack initiation, propagation and tensile overload stages, irrespective of the surface finish (see Fig. 13b and c). In both sample types, crack initiation was seen to occur at the surface, with none of the HED samples exhibiting a sub-surface origin for fatigue failure. This corroborates with the process parameters chosen for the manufacture of the samples, where the energy density has previously been found to induce an almost fully dense structure (>99 %) and therefore, little evidence of any process induced defects were observed on the fracture faces.

A similar behaviour is seen in the 45° samples, as depicted in Figs. 14-16. In each respective figure, high magnification images are given in the coloured boxes to represent features of interest within the fracture surfaces. Fig. 14 presents the fracture morphology of a LED as-built 45° sample that was again tested at $\varepsilon_a = 0.002$ mm/mm and failed after the shortest number of fatigue cycles (approximately 400 cycles) in comparison to other tests performed under the same conditions. Upon observing the fracture surface, there are strong indications as to why this sample failed prematurely. Like that seen in the LED 90° sample depicted in Fig. 13, the 45° equivalent also exhibits a significant presence of LoF powder particles, that appear to be located in a stepped-type manner running along the fracture surface, perpendicular to the direction of crack growth. Interestingly, despite the high population of defects in the sample, there is limited evidence of the fatigue crack initiating from a sub-surface location, Instead, it appears that the dominant factor promoting crack initiation is the as-built surface finish. As reported previously [20], an as-built surface roughness contains multiple high effective K_t factors which accelerate stage I fatigue (crack initiation) and the earlier onset of the stage II regime (crack propagation), leading to a reduction in the overall fatigue life. The location of crack nucleation is corroborated by the local presence of finely spaced striations (as given in the yellow box) that appear to emanate from the sample's surface. The narrow spacings between the striations indicate an initially slow rate of crack growth, which is predominantly dictated by the material's microstructural features, such as grain size, grain

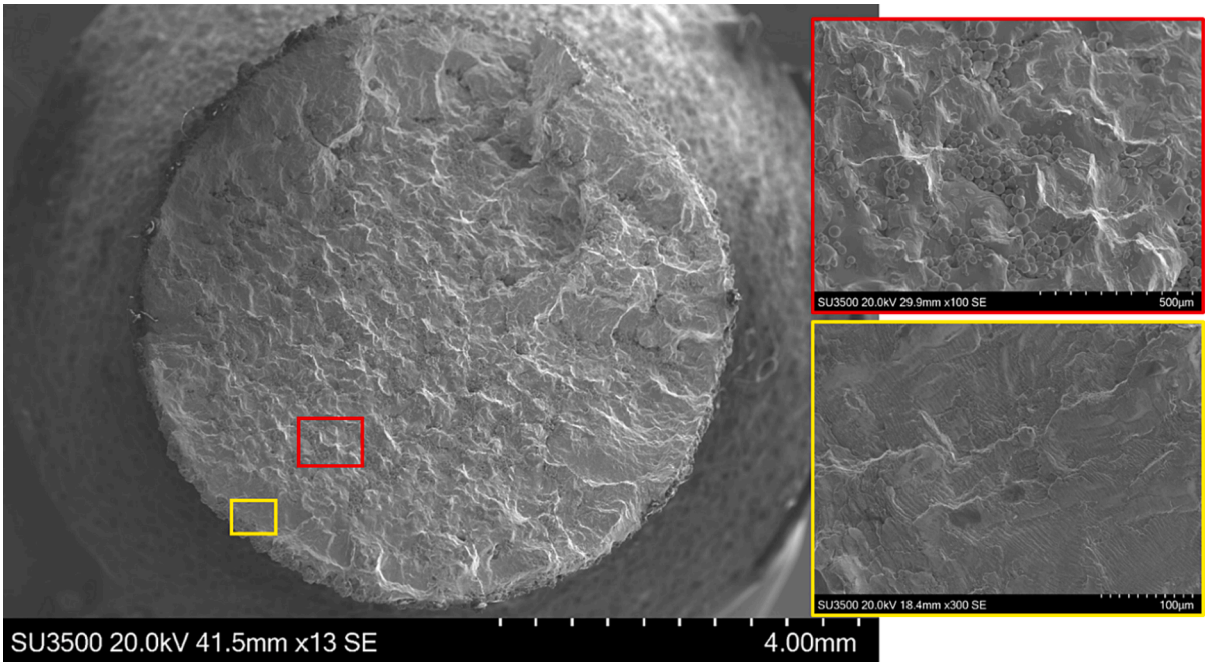

Fig. 14. SEM fracture surface of LPBF SS316L LED 45° as-built LCF sample.

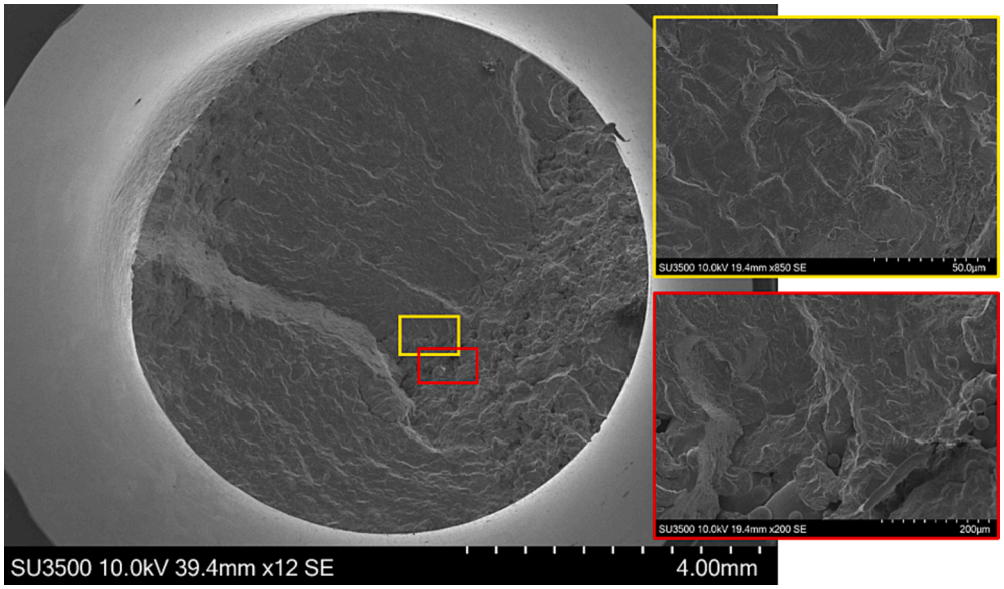

Fig. 15. SEM fracture surface of LPBF LED 45° SS316L longitudinally polished LCF sample.

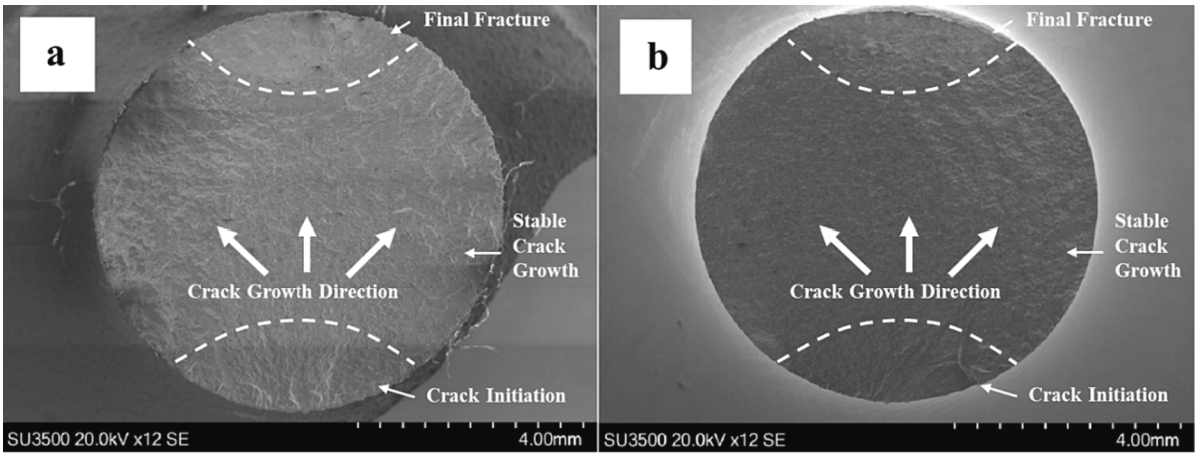

Fig. 16. SEM fracture surface of LPBF SS316L HED 45° LCF samples a) as-built, b) longitudinally polished.

morphology, crystallographic texture, the presence of strengthening phases and the externally applied load. However, such resistance will likely be eventually hindered by the quantity and population of LoF defects, which are present at a larger scale (approximately 30–50 μm in diameter, as shown in the red box) as compared to the grain size (approximately 20–30 μm in diameter). Therefore, grain boundaries would be expected to have a reduced effect in inhibiting crack growth, thus promoting a faster rate of crack propagation. As such, once the crack reaches a defective region in the sample, the rate of crack propagation accelerates and will further reduce the fatigue life of the material. Previously, Reimer et al. [19] stated that crack growth behaviour in LPBF SS316L is not significantly influenced by process-induced imperfections such as porosity. The major difference here though is likely to be the magnitude and volume of the defects found in the LED material, whereas the volume and geometry of the defects found in Reimer's research was not reported. Likewise, Zhang et al. [48] also found that LPBF SS316L material containing large porosity features is prone to porosity-driven crack initiation, which can significantly reduce the high cycle fatigue life, or those tested at low strain levels ($\varepsilon_a = < 0.003$ mm/mm).

This is in contrast to the behaviour seen in the polished LED 45° material (Fig. 15). In this sample, crack initiation has arisen from a subsurface location, situated towards the centre of the sample. Since the surface was subjected to a longitudinal polishing procedure, the as-built surface roughness has been removed to such an extent that it appears to play no role in the nucleation of the main fatigue crack. Instead, initiation appears to have occurred from a small cluster of LoF defects, as shown in the red box. Liang et al. [23] previously reported that through using the Murakami approach, that considers the relationship between fatigue strength and defect size as well as the fatigue strength ratio in different loading modes, multiple clustering defects can act synergistically as one large defect to initiate the fatigue crack. Detail on the striation behaviour is depicted within the yellow box.

Crack growth in the HED as-built and polished samples (Figure 16) appears to have initiated at the surface in both instances, since the material was fully dense. As would be expected, the presence of a polished surface offers a better fatigue performance compared to the as-built surfaces, due to the increased surface roughness. Likewise, the as-built HED samples are also outperformed by the LED polished samples, indicating that an as-built surface roughness plays a more influential role in controlling fatigue initiation behaviour than a sample containing isolated clusters of internal defects but with limited stress-raising features at the surface.

For the horizontally built samples, again, there was a significant

difference in the fracture morphology and this can be directly related to the energy densities used during manufacture. Fig. 17 presents the fracture surface of a LED 0° oriented sample and the images again show significant evidence of LoF features occurring (see yellow box), which appear to be aligned perpendicularly in a stepped arrangement across the surface (example shown in the red box). These are thought to relate to the build layers from the manufacturing process, where insufficient energy was used to melt the powder in the LED samples. Given the extent and population of these features, when subjected to a cyclic load, the dominant crack can propagate rapidly through such poorly consolidated material, resulting in a significantly shorter fatigue life compared to a fully dense equivalent.

The reduced energy density used in the manufacture of the LED samples is seen to result in LoF, high porosity, irregular fractures and poor fatigue performance. Despite these flaws, a selection of the LED samples appeared to have a density more comparable to the HED materials, as shown on the respective S-N plots and reported in Table 4. However, given that both sample sets were subjected to a HIP operation prior to mechanical testing, it appears that this has had little effect on improving the fatigue properties. Indeed, it has previously been reported that HIP operations can be detrimental to the fatigue performance of LPBF SS316L [19 49]. This was attributed to recrystallisation taking place in the microstructure since HIP procedures are typically performed at elevated temperature, which resulted in a significant reduction of the dislocation density and a 30 % drop in the yield strength [5051].

Zhang et al. [48] adopted the Kitagawa-Takahashi analysis to provide a theoretical estimate of the critical pore size in their work when investigating the fatigue behaviour of LPBF SS316L. The effect of layer thickness on the resulting fatigue performance was investigated, employing thicknesses of 20–80 μm, whilst keeping all the other main process parameters consistent. They found that for a layer thickness of between 40 and 60 μm (the layer thickness of the LED samples here is 50 μm), the critical pore size was found to lie between 13.4 and 53.6 μm. This range of values coincides with the powder size distribution (15–53 μm) of the material used in this study, thus indicating that a hollow powder particle or a single LoF defect can theoretically be considered to be critical and have an influence on the resulting fatigue behaviour of a given component. Caution should be taken however, since this value should be interpreted in conjunction with the size of the local microstructure. In the study by Zhang, the grain length was approximated to be between 30 and 40 μm, which is not too dissimilar to the sizes observed seen in the LED material in this investigation.

3.4. Coffin-Manson empirical modelling

Given that the presented results have been generated under LCF conditions, it is also of interest to determine whether empirical approaches can be accurately correlated to the different data sets whilst providing an indication of how the materials would perform under lower applied strain amplitudes. As employed in previous studies by the authors [20 22], the Coffin-Manson approach can be adopted to obtain empirically derived fatigue curves. The strain-based method utilises the data produced at the stabilised half-life condition to estimate the fatigue-life cyclic behaviour of the different material variants, through the following expression:

$$\frac{\Delta\varepsilon}{2} = \varepsilon_a = \frac{\Delta\varepsilon_e}{2} + \frac{\Delta\varepsilon_p}{2} = \frac{\sigma_f'}{E}(2N_f)^b + \varepsilon_f'(2N_f)^c \quad (3)$$

where $\frac{\Delta\varepsilon}{2}$ = total strain amplitude, $\frac{\Delta\varepsilon_e}{2}$ = elastic strain amplitude, $\frac{\Delta\varepsilon_p}{2}$ = plastic strain amplitude, σ_f' = fatigue strength coefficient, E = Young's Modulus, b = fatigue strength exponent, ε_f' = fatigue ductility coefficient, and c = fatigue ductility exponent. Further detail on how this expression is derived can be found in [20 22]. The calculated exponents and coefficients for the different material variants are presented in Table 7.

Plots of ε_a-N_f curves can then be obtained for the different material types, as displayed in Fig. 18. The predicted curves for the LED samples have been derived purely based on the samples that did not fail

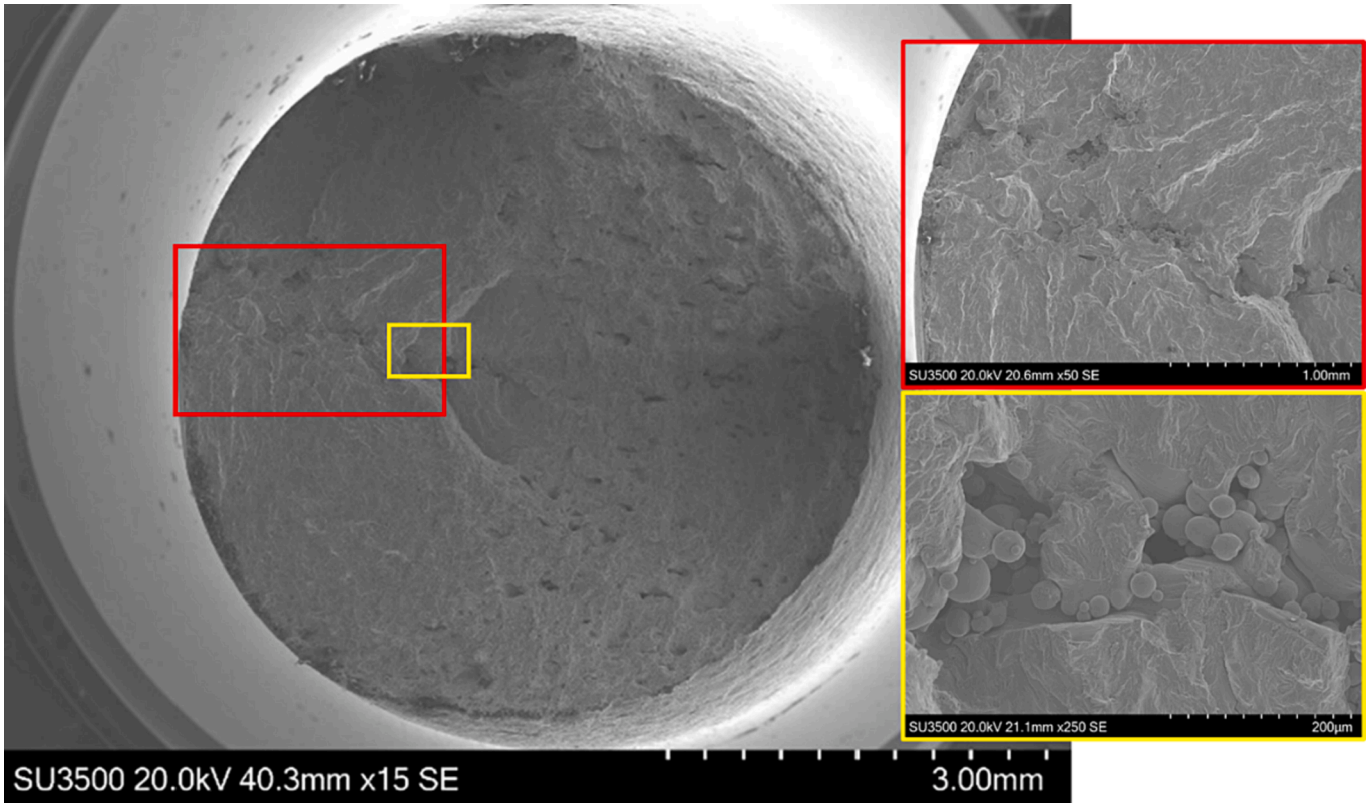

Fig. 17. SEM fracture surface of LPBF LED 0° SS316LN longitudinally polished LCF sample.

Table 7
Coffin-Manson curve fitting parameters for the different LPBF SS316L variants.

	HED					LED			
	90° P	90° AB	45° P	45° AB	0° P	90° AB	45° P	45° AB	0° P
σ_f'	806.5	615.93	796.04	673.06	719.76	508.78	558.12	258.27	643.23
b	−0.078	−0.067	−0.076	−0.067	−0.066	−0.048	−0.046	−0.056	−0.063
ε_f'	7.946	0.641	1.315	0.392	0.287	1.181	0.435	0.013	1.135
c	−0.790	−0.596	−0.657	−0.586	−0.510	−0.662	−0.532	−0.220	−0.655

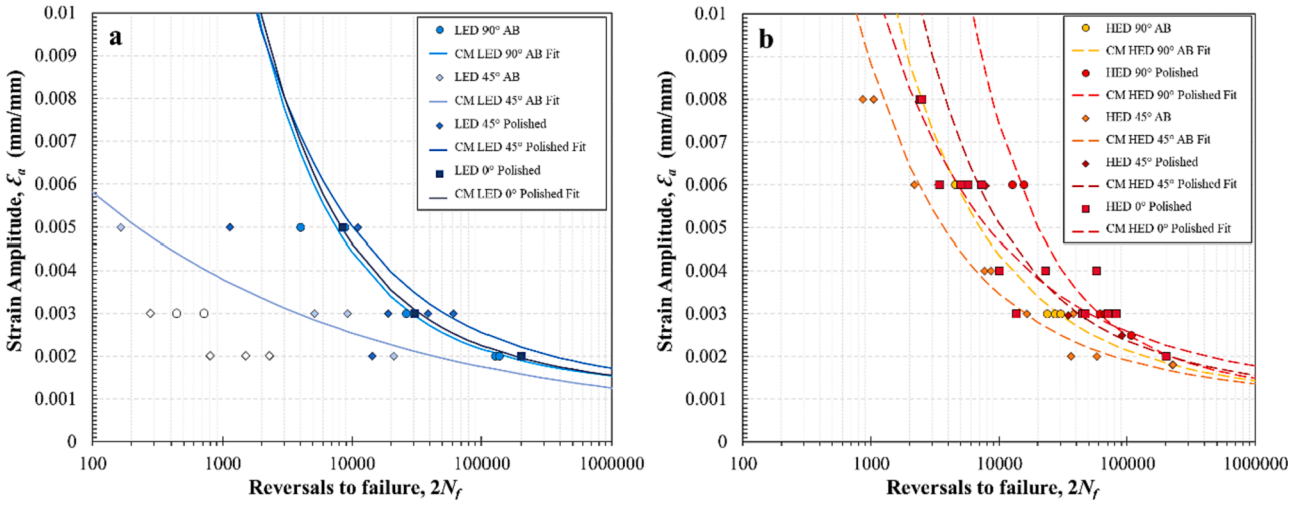

Fig. 18. Coffin-Manson fitting curves for LPBF SS316L samples, **a)** LED and **b)** HED variants.

prematurely (Fig. 18a)). As such, only the best performing data points for each LED material variant were included in the respective calculations. The samples that were not used for the empirically derived curves are indicated by a hollow data point.

The two plots show how the empirically derived curves correlate with the experimental data, and as can be seen, the results indicate a good agreement, and also provides an important indication of the estimated fatigue lives of the different material variants. Typically, due to the unpredictable nature of several LED samples (as indicated by the blue coloured series), many of the data points fall below the predicted fatigue curves. However, the empirical fits do provide an estimation of how those samples would behave under smaller strain amplitudes.

4. Conclusions

This study consisted of the manufacture of stainless steel 316L samples through LPBF and was aimed at investigating the influence of build orientation and volumetric energy density on the resulting mechanical performance under low cycle fatigue conditions. Advanced microscopy, surface roughness profiling, fractographic investigations and empirical modelling have enabled the following conclusions to be drawn:

- A high volumetric energy density (HED) (100.03 J/mm^3) used during LPBF manufacture was found to induce a typical microstructure associated with AM, including an elongated grain morphology in the epitaxial build direction, with high levels of anisotropy and texture aligned to the ⟨1 0 1⟩ direction..
- The higher energy density enabled a fully dense structure (>99 %) to be formed, however, the low energy density samples contained a large quantity of LoF defects leading to a final structural density in some cases of much less relative density, despite both material types being subjected to the same post-manufacture HIP procedure. This was attributed to the contrasting environments used during manufacture (argon in LED, nitrogen in HED samples), since argon is insoluble during HIP and becomes trapped in the final structure. Instead, the HIP procedure had a negative impact on the LCF behaviour of the LED samples, promoting an increase in grain size due to the high temperature used, which induced further grain growth.
- Samples manufactured using a low energy density (LED) (54.5 J/mm^3) exhibited a more refined and equiaxed grain structure, with less anisotropy and crystallographic texture, all of which are desired when designing a material to resist cyclic deformation. However, all of these beneficial factors are overcome by the significant presence of LoF defects which could not be fully eradicated during HIP.
- The HED samples were found to have more severe effective stress concentration factors at the surface than the LED material in the as-built condition, particularly in the vertical, 90° orientation. However, since the internal bulk material contained significant porosity in the form of LoF defects, the LED samples generally had an inferior fatigue response. This was evidenced in the contrasting fracture morphologies seen in the two material types, where fatigue damage of LED samples containing a high population of defects was found to originate from a subsurface feature, whereas in the HED samples, fatigue initiation solely occurred at the surface, irrespective of the surface finish.
- In both LED and HED batches, polished samples significantly outperformed the as-built equivalents, but this deficit is reduced if the material contains clusters of internal stress raising defects, which effectively synergistically act as a single large defect to induce fatigue initiation.
- The Coffin-Manson empirical fatigue-lifing approach has been found to appropriately capture the LCF behaviour of LPBF SS316LN samples built in alternative build orientations for both LED and HED material variants. The LED samples that failed prematurely during

LCF testing fell below the predicted curve, but the empirically derived prediction provided a suitable estimation of LED material consisting of less structural defects.

- To obtain a more optimal resistance to LCF damage through a refined equiaxed grain structure with little anisotropy and microstructural texture, a future recommendation would be to manufacture a series of experimental coupons with a low energy density and a slightly reduced layer thickness, but within a nitrogen atmosphere. This would produce an intentionally porous structure but with a fine microstructure with limited texture and a more favourable as-built surface roughness, all of which is produced in a faster manufacturing process with a higher production rate. Post-manufacture, the HIP process would then be envisaged to consolidate a large element of the material, but caution should be taken as this may be to the detriment of the dimensional accuracy of the final component.

CRediT authorship contribution statement

Rory Douglas: Writing – review & editing, Writing – original draft, Validation, Investigation, Formal analysis. **William Beard:** Validation, Investigation, Formal analysis. **Nicholas Barnard:** Writing – review & editing, Investigation. **Seungjong Lee:** Methodology, Investigation. **Shuai Shao:** Writing – review & editing, Methodology. **Nima Shamsaei:** Writing – review & editing, Supervision, Methodology, Conceptualization. **Thomas Jones:** Writing – review & editing, Supervision, Methodology, Conceptualization. **Robert Lancaster:** Writing – review & editing, Supervision, Project administration, Methodology, Funding acquisition, Conceptualization.

Declaration of Competing Interest

The authors declare that they have no known competing financial interests or personal relationships that could have appeared to influence the work reported in this paper.

Data availability

The data that has been used is confidential.

Acknowledgements

The current research was funded under the EPSRC Industrial Case Award EP/T517537/1. The provision of a research bursary, materials, and supporting information from Rolls-Royce plc. is gratefully acknowledged. Mechanical tests were performed at Swansea Materials Research and Testing Ltd. (SMaRT).

References

[1] Bhadeshia H, Honeycombe R. Stainless Steel. In: Steels: Microstructure and Properties. Elsevier; 2017. p. 343–76. https://doi.org/10.1016/B978-0-08-100270-4.00012-3.
[2] Esfahani MN, Coupland J, Marimuthu S. Microstructure and mechanical properties of a laser welded low carbon–stainless steel joint. J Mater Process Technol Dec. 2014;214(12):2941–8. https://doi.org/10.1016/j.jmatprotec.2014.07.001.
[3] Pawar SS, Bera TC, Sangwan KS. Modelling of energy consumption for milling of circular geometry. Procedia CIRP 2021;98:470–5. https://doi.org/10.1016/j.procir.2021.01.136.
[4] Praveena BA, Lokesh N, Abdulrajak B, Santhosh N, Praveena BL, Vignesh R. A comprehensive review of emerging additive manufacturing (3D printing technology): Methods, materials, applications, challenges, trends and future potential. Mater Today Proc 2022;52:1309–13. https://doi.org/10.1016/j.matpr.2021.11.059.
[5] Marrey M, Malekipour E, El-Mounayri H, Faierson EJ. A Framework for Optimizing Process Parameters in Powder Bed Fusion (PBF) Process Using Artificial Neural Network (ANN). Procedia Manuf 2019;34:505–15. https://doi.org/10.1016/j.promfg.2019.06.214.
[6] Leicht A, Rashidi M, Klement U, Hryha E. Effect of process parameters on the microstructure, tensile strength and productivity of 316L parts produced by laser powder bed fusion. Mater Charact Jan. 2020;159:110016. https://doi.org/10.1016/j.matchar.2019.110016.
[7] Poudel A, Yasin MS, Ye J, Liu J, Vinel A, Shao S, et al. Feature-based volumetric defect classification in metal additive manufacturing. Nat Commun Oct. 2022;13(1). https://doi.org/10.1038/s41467-022-34122-x.
[8] Zhang M, Sun C-N, Zhang X, Goh PC, Wei J, Hardacre D, et al. Fatigue and fracture behaviour of laser powder bed fusion stainless steel 316L: Influence of processing parameters. Mater Sci Eng A 2017;703:251–61.
[9] Ponticelli GS, Panciroli R, Venettacci S, Tagliaferri F, Guarino S. Experimental investigation on the fatigue behavior of laser powder bed fused 316L stainless steel. CIRP J Manuf Sci Technol Aug. 2022;38:787–800. https://doi.org/10.1016/j.cirpj.2022.07.007.
[10] Pegues JW, Shao S, Shamsaei N, Sanaei N, Fatemi A, Warner DH, et al. Fatigue of additive manufactured Ti-6Al-4V, Part I: The effects of powder feedstock, manufacturing, and post-process conditions on the resulting microstructure and defects. Int J Fatigue 2020;132:105358.
[11] Ahmed N, Barsoum I, Haidemenopoulos G, Al-Rub RKA. Process parameter selection and optimization of laser powder bed fusion for 316L stainless steel: A review. J Manuf Process Mar. 2022;75:415–34. https://doi.org/10.1016/j.jmapro.2021.12.064.
[12] Sun Z, Tan X, Tor SB, Yeong WY. Selective laser melting of stainless steel 316L with low porosity and high build rates. Mater Des Aug. 2016;104:197–204. https://doi.org/10.1016/j.matdes.2016.05.035.
[13] Shrestha R, Shamsaei N, Seifi M, Phan N. An investigation into specimen property to part performance relationships for laser beam powder bed fusion additive manufacturing. Addit Manuf Oct. 2019;29:100807. https://doi.org/10.1016/j.addma.2019.100807.
[14] Soltani-Tehrani A, Shrestha R, Phan N, Seifi M, Shamsaei N. Establishing specimen property to part performance relationships for laser beam powder bed fusion additive manufacturing. Int J Fatigue Oct. 2021;151:106384. https://doi.org/10.1016/j.ijfatigue.2021.106384.
[15] Sinha S, Szpunar JA, Kiran Kumar NAP, Gurao NP. Tensile deformation of 316L austenitic stainless steel using in-situ electron backscatter diffraction and crystal plasticity simulations. Mater Sci Eng A 2015;637:48–55.
[16] Shin W-S, Son B, Song W, Sohn H, Jang Ho, Kim Y-J, et al. Heat treatment effect on the microstructure, mechanical properties, and wear behaviors of stainless steel 316L prepared via selective laser melting. Mater Sci Eng A 2021;806:140805.
[17] Yu J, Kim D, Ha K, Jeon JB, Lee W. Strong feature size dependence of tensile properties and its microstructural origin in selectively laser melted 316L stainless steel. Mater Lett Sep. 2020;275:128161. https://doi.org/10.1016/j.matlet.2020.128161.
[18] Song Y, Sun Q, Guo K, Wang X, Liu J, Sun J. Effect of scanning strategies on the microstructure and mechanical behavior of 316L stainless steel fabricated by selective laser melting. Mater Sci Eng A Aug. 2020;793:139879. https://doi.org/10.1016/j.msea.2020.139879.
[19] Riemer A, Leuders S, Thöne M, Richard HA, Tröster T, Niendorf T. On the fatigue crack growth behavior in 316L stainless steel manufactured by selective laser melting. Eng Fract Mech Apr. 2014;120:15–25. https://doi.org/10.1016/j.engfracmech.2014.03.008.
[20] Beard W, Lancaster R, Barnard N, Jones T, Adams J. The influence of surface finish and build orientation on the low cycle fatigue behaviour of laser powder bed fused stainless steel 316L. Mater Sci Eng A Feb. 2023;864:144593. https://doi.org/10.1016/j.msea.2023.144593.
[21] Avanzini A. Fatigue Behavior of Additively Manufactured Stainless Steel 316L. Materials Dec. 2022;16(1):65. https://doi.org/10.3390/ma16010065.
[22] Shrestha R, Simsiriwong J, Shamsaei N. Fatigue behavior of additive manufactured 316L stainless steel parts: Effects of layer orientation and surface roughness. Addit Manuf 2019;28:23–38.
[23] Liang X, Hor A, Robert C, Salem M, Lin F, Morel F. High cycle fatigue behavior of 316L steel fabricated by laser powder bed fusion: Effects of surface defect and loading mode. Int J Fatigue Jul. 2022;160:106843. https://doi.org/10.1016/j.ijfatigue.2022.106843.
[24] ASTM E 606, 'Standard Practice for Strain-Controlled Fatigue Testing', Astm. 2010.
[25] Atkinson HV, Davies S. Fundamental aspects of hot isostatic pressing: An overview. Metall Mater Trans A Dec. 2000;31(12):2981–3000. https://doi.org/10.1007/s11661-000-0078-2.
[26] 'ISO 21920-3:2021. Geometrical product specifications (GPS) — Surface texture: Profile — Part 3: Specification operators', ISO. 2021.
[27] Snow Z, Nassar AR, Reutzel EW. Invited Review Article: Review of the formation and impact of flaws in powder bed fusion additive manufacturing. Addit Manuf 2020;36(January). https://doi.org/10.1016/j.addma.2020.101457. 101457.
[28] DebRoy T, Wei HL, Zuback JS, Mukherjee T, Elmer JW, Milewski JO, et al. Additive manufacturing of metallic components – Process, structure and properties. Prog Mater Sci 2018;92:112–224.
[29] Shao S, Mahtabi MJ, Shamsaei N, Thompson SM. Solubility of argon in laser additive manufactured α-titanium under hot isostatic pressing condition. Comput Mater Sci Apr. 2017;131:209–19. https://doi.org/10.1016/j.commatsci.2017.01.040.
[30] Fleischmann B, Chateau-Cornu J-P, Dembinski L, Gyss O, Bigot R, Danlos Y, et al. Influence of particle size on surface oxide of 316L stainless steel powders for hot isostatic pressing. Materialia (Oxf) 2022;22:101405.
[31] Ruttert B, Ramsperger M, Roncery LM, Lopez-galilea I, Körner C, Theisen W. Impact of hot isostatic pressing on microstructures of CMSX-4 Ni-base superalloy fabricated by selective electron beam melting. JMADE 2016;110:720–7. https://doi.org/10.1016/j.matdes.2016.08.041.

[32] Mower TM, Long MJ. Materials Science & Engineering A Mechanical behavior of additive manufactured, powder-bed laser-fused materials. Mater Sci Eng A 2016; 651:198–213. https://doi.org/10.1016/j.msea.2015.10.068.
[33] Lavery NP, Cherry J, Mehmood S, Davies H, Girling B, Sackett E, et al. Effects of hot isostatic pressing on the elastic modulus and tensile properties of 316L parts made by powder bed laser fusion. Mater Sci Eng A 2017;693:186–213.
[34] Valente EH, Nadimpalli VK, Andersen SA, Pederson DB, Christiansen TL, Somers MAJ. Influence of atmosphere on microstructure and nitrogen content in AISI 316L fabricated by laserbased powder bed. Proceedings of the 19th International Conference and Exhibition (EUSPEN 2019), Bilbao. 2019.
[35] Röttger A, Geenen K, Windmann M, Binner F, Theisen W. Comparison of microstructure and mechanical properties of 316 L austenitic steel processed by selective laser melting with hot-isostatic pressed and cast material. Mater Sci Eng A Dec. 2016;678:365–76. https://doi.org/10.1016/j.msea.2016.10.012.
[36] Grech IS, Sullivan JH, Lancaster RJ, Plummer J, Lavery NP. The optimisation of hot isostatic pressing treatments for enhanced mechanical and corrosion performance of stainless steel 316L produced by laser powder bed fusion. Addit Manuf Oct. 2022;58:103072. https://doi.org/10.1016/j.addma.2022.103072.
[37] Nezhadfar PD, Anderson-Wedge K, Daniewicz SR, Phan N, Shao S, Shamsaei N. Improved high cycle fatigue performance of additively manufactured 17–4 PH stainless steel via in-process refining micro-/defect-structure. Addit Manuf Dec. 2020;36:101604. https://doi.org/10.1016/j.addma.2020.101604.
[38] Hatami S, Ma T, Vuoristo T, Bertilsson J, Lyckfeldt O. Fatigue Strength of 316 L Stainless Steel Manufactured by Selective Laser Melting. J Mater Eng Perform May 2020;29(5):3183–94. https://doi.org/10.1007/s11665-020-04859-x.
[39] Cherry JA, Davies HM, Mehmood S, Lavery NP, Brown SGR, Sienz J. Investigation into the effect of process parameters on microstructural and physical properties of 316L stainless steel parts by selective laser melting. Int J Adv Manuf Technol Feb. 2015;76(5–8):869–79. https://doi.org/10.1007/s00170-014-6297-2.
[40] Narasimharaju SR, Zeng W, See TL, Zhu Z, Scott P, Jiang X, et al. A comprehensive review on laser powder bed fusion of steels: Processing, microstructure, defects and control methods, mechanical properties, current challenges and future trends. J Manuf Process 2022;75:375–414.
[41] Tian Y, Tomus D, Rometsch P, Wu X. Influences of processing parameters on surface roughness of Hastelloy X produced by selective laser melting. Addit Manuf 2017;13:103–12. https://doi.org/10.1016/j.addma.2016.10.010.
[42] Yadollahi A, Shamsaei N. Additive manufacturing of fatigue resistant materials: Challenges and opportunities. Int J Fatigue May 2017;98:14–31. https://doi.org/10.1016/j.ijfatigue.2017.01.001.
[43] Elangeswaran C, Cutolo A, Muralidharan GK, de Formanoir C, Berto F, Vanmeensel K, et al. Effect of post-treatments on the fatigue behaviour of 316L stainless steel manufactured by laser powder bed fusion. Int J Fatigue 2019;123: 31–9.
[44] Pegues J, Roach M, Scott Williamson R, Shamsaei N. Surface roughness effects on the fatigue strength of additively manufactured Ti-6Al-4V. Int J Fatigue Nov. 2018; 116:543–52. https://doi.org/10.1016/j.ijfatigue.2018.07.013.
[45] Pegues JW, Shamsaei N, Roach MD, Williamson RS. Fatigue life estimation of additive manufactured parts in the as-built surface condition. Mater Des Process Commun Jun. 2019;1(3). https://doi.org/10.1002/mdp2.36.
[46] Garlea E, Choo H, Sluss CC, Koehler MR, Bridges RL, Xiao X, et al. Variation of elastic mechanical properties with texture, porosity, and defect characteristics in laser powder bed fusion 316L stainless steel. Mater Sci Eng A 2019;763:138032.
[47] Vallejo ND, Kljestan N, Ayers N, Knezevic M, Sohn Y. Flaw type dependent tensile properties of 316L stainless steel additively manufactured by laser powder bed fusion. Results Mater Sep. 2022;15:100315. https://doi.org/10.1016/j.rinma.2022.100315.
[48] Zhang M, et al. Competing Influence of Porosity and Microstructure on the Fatigue Property of Laser Powder Bed Fusion Stainless Steel 316L. Solid Freeform Fabrication 2017: Proceedings of the 28th Annual International Solid Freeform Fabrication Symposium – An Additive Manufacturing Conference, Austin, Texas. 2017.
[49] Leuders S, Lieneke T, Lammers S, Tröster T, Niendorf T. On the fatigue properties of metals manufactured by selective laser melting – The role of ductility. J Mater Res Sep. 2014;29(17):1911–9. https://doi.org/10.1557/jmr.2014.157.
[50] Kong D, Dong C, Ni X, Zhang L, Yao J, Man C, et al. Mechanical properties and corrosion behavior of selective laser melted 316L stainless steel after different heat treatment processes. J Mater Sci Technol 2019;35(7):1499–507.
[51] Kong D, Ni X, Dong C, Lei X, Zhang L, Man C, et al. Bio-functional and anti-corrosive 3D printing 316L stainless steel fabricated by selective laser melting. Mater Des 2018;152:88–101.